A second-order extension of a robust implicit-explicit acoustic-transport splitting scheme for two-phase flows

Lucas Tallois, Simon Peluchon, Philippe Villedieu

To cite this version:

Lucas Tallois, Simon Peluchon, Philippe Villedieu. A second-order extension of a robust implicit-explicit acoustic-transport splitting scheme for two-phase flows. Computers and Fluids, 2022, 244, pp.105531. 10.1016/j.compfluid.2022.105531 . hal-03722371

HAL Id: hal-03722371
https://hal.science/hal-03722371v1

A second-order extension of a robust implicit–explicit acoustic-transport splitting scheme for two-phase flows

Lucas Tallois[a,c,*], Simon Peluchon[a], Philippe Villedieu[c,b]

[a] *CEA-CESTA, 15 avenue des sablières - CS 60001, 33116 Le Barp Cedex, France.*
[b] *ONERA/DMPE, Université de Toulouse, F-31055 Toulouse, France.*
[c] *INSA, 135 Avenue de Rangueil, 31400 Toulouse, France.*

Abstract

Diffuse interface methods have proven their ability to simulate complex two-phase flows. A number of robust numerical schemes have been developed to simulate such flows involving large density and pressure ratios. Diffusion induced by these methods, however, makes it difficult to localize the interface between the two fluids. To overcome this issue, while retaining the advantages of diffuse interface methods, a second-order extension using a Monotonic Upstream-centered Scheme for Conservation Laws-type (MUSCL-type) method of the implicit–explicit acoustic-transport splitting scheme introduced in [40] is presented. A specific compressive limiter is used for the volume fraction in order to limit the diffusion of the interface between the two fluids.

Numerical simulations are presented to illustrate the capability of the proposed new method to simulate highly complex compressible two-phase flows.

Keywords: Two-phase flows, MUSCL, Unstructured meshes, Implicit, Compressive limiter

1. Introduction

This work takes place in the context of liquid ablation. When an object enters the atmosphere at very high speed (see Fig. 1), it is subjected to significant heat flux which may degrade its structure. Depending on its composition, the object may sublimate or liquefy. Thus, when a liquid phase appears, it is necessary to deal with the flow of both the liquid and gas phases by an appropriate model.

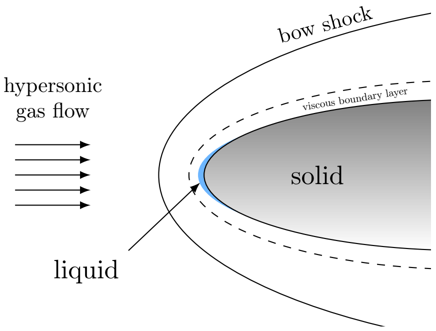

Figure 1: Schematic representation of an object entering the atmosphere.

The modelling of two-phase flows has been the subject of numerous studies. Several methods have been developed, each with advantages and disadvantages. They can be grouped into two distinct families: the sharp interface methods and the diffuse interface methods.

Among these methods, the first one is the so-called Lagrangian method [52]. Each phase can be modeled with different equations, and the interface is followed explicitly by moving the mesh at the material speed. In the so-called ALE methods (Arbitrary Lagrangian-Eulerian methods), the mesh follows the displacement of the interface. The mesh can, however, be subject to strong distortions that can impact the robustness of the calculations.

Moreover, among the Eulerian methods with no or almost no diffusion, there are the Front capturing methods as Volume Of Fluid (VOF) [27] and Moment Of Fluid (MOF) [1] methods, the Front tracking methods [9] and the Level Set method [38]. Although widely used for their satisfactory results, these methods are complex to implement and some may be not conservative, which can be a serious drawback depending on the targeted applications.

Diffuse interface methods, on the other hand, are based on two-phase models, i.e. models containing conservation equations for each of the two phases that are artificially assumed to be present at any point in space. The equations are solved on a fixed mesh in a Eulerian manner. The same equations are solved over the whole domain. These methods allow the diffusion of the interface between each fluid. Thus, mixing zones appear, corresponding to a numerical spreading of the interface over a few cells. These areas require special processing to preserve the thermodynamic consistency of the model. Many studies have been carried

---

[*] Corresponding author.
Email addresses: `lucas.tallois@cea.fr` (Lucas Tallois), `simon.peluchon@cea.fr` (Simon Peluchon), `philippe.villedieu@onera.fr` (Philippe Villedieu)

Preprint submitted to Elsevier *July 12, 2022*

out with the aim of developing two-phase models, following the work of Baer & Nunziato [4] and their seven-equation model. Indeed, there is a whole hierarchy of two-phase models deduced from the seven-equation model [19, 33]. A local velocity equilibrium between the two fluids [45] allows us to reduce to a six-equation model. If the equilibrium of the pressures is assumed, the five-equation model of Kapila et al. [29, 31] or the reduced five-equation model of [2, 35, 36] can be obtained.

Another approach to simulate two-phase flow consists in writing the same set of equations for each fluid, and to close the model by defining the mixing quantities as the quantities of each fluid weighted by its volume fraction [13, 23, 7]. An isobaric closure assumption and the resolution of a 2×2 system allows the volume fraction in the mixing region to be determined.

Another approach existing in the class of diffuse interface methods is the phase field method [3, 25]. This method introduces an auxiliary field (the phase field or color function) that acts as an order parameter taking two distinct values in each of the phases, with a smooth change between the two values in the area around the interface. In two-phase flow models, the notion of color function or phase field parameter is not explicitly introduced but its role is implicitly played by the volume fraction of one of the two fluids.

In this work, a diffuse interface method based on a two-phase flow model is considered. The advantages of such method are numerous: the same equations are solved over the whole domain, interfaces do not require any specific processing and appearance of new interfaces as well as the changes of topology are achieved naturally. In the case where one wishes to model the two-phase flow between a gaseous phase and a liquid phase, where the second phase is not present initially and appears from solid fusion, these methods seem the most relevant and the easiest to implement. The counterpart of these methods is the diffusion of the interface between the two fluids, which can deteriorate the solution when the fluids are immiscible. Each of the fluids is assumed to be present at any point in space, with a volume fraction very close to 0 or 1 depending on whether we are in fluid 1 or fluid 2. It is only in the vicinity of the interface between the fluids that the volume fraction of each of the fluids pass through the value $1/2$. Since we do not consider that fluids slide relative to each other at the mesh scale, a two-phase model with one velocity and one pressure is used. This avoids having to consider a model with two velocities and two pressures [4] which poses greater theoretical and numerical difficulties and is not necessary when the mixing zone is purely numerical and as fine as possible, and does not model a zone with inclusions such as drops or bubbles of a size smaller than the scale resolved by the mesh. As the two phases are not initially mixed, the non-conservative term in the Kapila et al. model [29, 31] is null. The reduced five-equation model of [2, 35] will therefore be used in this work. Several methods have been developed in order to limit this numerical diffusion of the interface. Kokh and Lagoutière used the anti-diffusive scheme [30] developed in [18], which consists in using a flux as downwind as possible, while guaranteeing the stability and consistency of the scheme. This method limits the diffusion of the interface to 2 mixture cells. Jung et al. [26] combined the Glimm's random projection method near the material interface with the upwind scheme to simulate two-phase flow without any diffusion cells. They extended this method to the second order in space and time. Extension to higher dimension is achieved with directional splitting. Shyue and Xiao [47] adapted the THINC method of [53] as a sharpening technique to simulate two-phase flows. The main idea is to reconstruct the solution with the hyperbolic tangent function, controlling the compressive character of the reconstruction with a β-parameter. This is widely combined with the Boundary Variation Diminishing algorithm [48, 17, 14] to simulate two-phase flows on structured and unstructured grids. In the context of MUSCL-type schemes [32], where flux are computed with piecewise linear reconstruction with slope limitation, slope limiters can be designed to have compressive properties and give a sharp interface when applied to the volume fraction transport equation. This approach has been widely used in the literature as for instance in Qian et al. [42], Blanchard [7], Chiapolino et al. [15] and De Vuyst et al. [16].

This paper is an extension of the work presented in [40] where the splitting strategy of [10] is used to solve the five-equation system of [35, 2]. The strategy consists in solving the acoustic part with an implicit scheme while the transport step is solved explicitly. The effects related to heat dissipation and viscosity can be easily added to the first step [41], which justifies its implicit treatment. We will focus here only on the hyperbolic part of the equations. The aim is to increase the accuracy of the first-order method described in [40] and to improve the resolution of the material interface. A MUSCL-type scheme on an unstructured grid is used, in order to improve the accuracy of the numerical scheme. A strategy to improve the resolution of the two-phase interface on an unstructured grid is employed. Indeed, the method must be able to handle a body-fitted mesh composed of quadrilaterals and deformed by the ablation. In the context of the splitting strategy, a new and more accurate implicit-explicit time-scheme is presented.

The paper is organized as follows. First, the governing equations used to simulate two-phase flow are introduced and the first order numerical scheme is briefly recalled in Section 2. Then, a second-order in space extension and improvement of the time scheme are derived in Section 3. Some numerical results are presented in Section 4.

2. Model and numerical scheme

2.1. The five-equation system

We denote by ρ_k, ε_k and p_k the density, internal energy and pressure of fluid $k = 1, 2$. Each fluid is equipped with an Equation Of State (EOS) of the form $p_k = p_k(\rho_k, \varepsilon_k)$. The volume fraction z_k, such that $z_1 + z_2 = 1$, allows the position of the interface to be located. In the sequel, we denote by $z = z_1$ the volume fraction of the first fluid. The mixture density and internal energy are given by

$$\begin{aligned} \rho &= \rho_1 z + \rho_2(1-z), \\ \rho\varepsilon &= \rho_1\varepsilon_1 z + \rho_2\varepsilon_2(1-z). \end{aligned} \tag{2.1}$$

Both fluids share the same velocity $\boldsymbol{u}$ and the same pressure p. The five-equation system of [2, 35] for non-miscible fluids with isobaric closure reads

$$\begin{cases} \partial_t(\rho_1 z) & + \quad \nabla\cdot(\rho_1 z\boldsymbol{u}) & = 0, \\ \partial_t(\rho_2(1-z)) & + \quad \nabla\cdot(\rho_2(1-z)\boldsymbol{u}) & = 0, \\ \partial_t(\rho\boldsymbol{u}) & + \quad \nabla\cdot(\rho\boldsymbol{u}\otimes\boldsymbol{u}) + \boldsymbol{\nabla} p & = \boldsymbol{0}, \\ \partial_t(\rho E) & + \quad \nabla\cdot(\rho E\boldsymbol{u} + p\boldsymbol{u}) & = 0, \\ \partial_t z & + \quad \boldsymbol{u}\cdot\nabla z & = 0, \end{cases} \tag{2.2}$$

where $E = \varepsilon + \frac{||\boldsymbol{u}||^2}{2}$ is the total energy of the two-fluid media.

Each fluid is considered to be governed by a stiffened gas EOS, since we consider flows with a liquid phase and a gas phase. The EOS of phase k thus reads

$$p_k = \rho_k\varepsilon_k(\gamma_k - 1) - \gamma_k\pi_k, \tag{2.3}$$

where $\gamma_k > 1$ is the adiabatic exponent and $\pi_k \geq 0$ is a reference pressure. Note that perfect gas EOS is obtained with $\pi_k = 0$. The mixture pressure p is the solution of the system

$$\begin{cases} p_1(\rho_1, \varepsilon_1) = p_2(\rho_2, \varepsilon_2), \\ \rho\varepsilon = \rho_1\varepsilon_1 z + \rho_2\varepsilon_2(1-z). \end{cases} \tag{2.4}$$

In the case of two stiffened gases, (2.4) can be solved explicitly and we get the following expression for the mixture pressure

$$p = \rho\varepsilon(\gamma - 1) - \gamma\pi, \tag{2.5}$$

where the adiabatic exponent mixture γ and the reference pressure π are given by

$$\gamma = 1 + \frac{1}{\sum\limits_{k=1}^{2} \frac{z_k}{\gamma_k - 1}} \quad \text{and} \quad \pi = \frac{\gamma - 1}{\gamma}\sum_{k=1}^{2}\frac{z_k\gamma_k\pi_k}{\gamma_k - 1}. \tag{2.6}$$

The speed of sound c_k of each phase is defined by $c_k^2 = \frac{\partial p_k}{\partial \rho_k}|_{s_k}$, where s_k is the entropy. The mixture sound speed for two stiffened gas reads

$$c^2 = \gamma\frac{p + \pi}{\rho}. \tag{2.7}$$

Note before going further that the system (2.2) can be written, introducing the mass fraction of the first fluid $y = \frac{\rho_1 z}{\rho}$, in the following form

$$\begin{cases} \partial_t\rho & + \quad \nabla\cdot(\rho\boldsymbol{u}) & = 0, \\ \partial_t(\rho y) & + \quad \nabla\cdot(\rho y\boldsymbol{u}) & = 0, \\ \partial_t(\rho\boldsymbol{u}) & + \quad \nabla\cdot(\rho\boldsymbol{u}\otimes\boldsymbol{u}) + \boldsymbol{\nabla} p & = \boldsymbol{0}, \\ \partial_t(\rho E) & + \quad \nabla\cdot(\rho E\boldsymbol{u} + p\boldsymbol{u}) & = 0, \\ \partial_t z & + \quad \boldsymbol{u}\cdot\nabla z & = 0. \end{cases} \tag{2.8}$$

The evolution equation of ρ is obtained by summing the evolution equation of $\rho_1 z_1$ and $\rho_2 z_2$ of system (2.2). The evolution equation of ρy is nothing but the evolution equation of $\rho_1 z_1$ by definition. This form allows us to write in the Lagrangian form the acoustic step, described below.

Remark 1
If the volume fraction only takes the values 0 and 1, then (2.8) is equivalent to the 4-equation model i.e (2.8) without the equation on ρy.

2.2. Splitting strategy

We will briefly recall the method of solving the five-equation system, where a detailed approach is described in [40]. The expansion of system (2.8) reads

$$\begin{cases} \partial_t\rho & + \quad \rho\nabla\cdot\boldsymbol{u} & + \quad \boldsymbol{u}\cdot\nabla\rho & = 0, \\ \partial_t(\rho y) & + \quad \rho y\nabla\cdot\boldsymbol{u} & + \quad \boldsymbol{u}\cdot\nabla(\rho y) & = 0, \\ \partial_t(\rho\boldsymbol{u}) & + \quad \rho\boldsymbol{u}\nabla\cdot\boldsymbol{u} + \boldsymbol{\nabla} p & + \quad \boldsymbol{u}\cdot\nabla(\rho\boldsymbol{u}) & = \boldsymbol{0}, \\ \partial_t(\rho E) & + \quad \rho E\nabla\cdot\boldsymbol{u} + \nabla\cdot(p\boldsymbol{u}) & + \quad \boldsymbol{u}\cdot\nabla(\rho E) & = 0, \\ \partial_t z & & + \quad \boldsymbol{u}\cdot\nabla z & = 0. \end{cases} \tag{2.9}$$

The five-equation system is then split into two subsystems [10, 11, 40]. The first system contains only the acoustic waves, while the second system takes into account the propagation of material waves through the fluid.

The system corresponding to the acoustic step is hyperbolic with eigenvalues 0 and $\pm c$. It is rewritten and then solved in its Lagrangian form, which reads

$$\partial_t\boldsymbol{V} + \vartheta\nabla\cdot\boldsymbol{G}(\boldsymbol{V}) = 0, \tag{2.10}$$

where $\boldsymbol{V} = (\vartheta, y, \boldsymbol{u}, E, z)$ are the Lagrangian variables, $\boldsymbol{G}(\boldsymbol{V}) = (\boldsymbol{u}, 0, p, p\boldsymbol{u}, 0)$ is the flux and $\vartheta = 1/\rho$ is the specific volume. Note that during this step, volume fraction and mass fraction are not modified.

The transport step system, where the propagation speed is only $\boldsymbol{u}$, reads

$$\partial_t\boldsymbol{U} + \boldsymbol{u}\nabla\cdot\boldsymbol{U} = 0, \tag{2.11}$$

with $\boldsymbol{U} = (\rho, \rho y, \rho\boldsymbol{u}, \rho E, z)$ the conservative variables.

2.3. Numerical scheme

Let us first consider a domain $\Omega \in \mathbb{R}^2$ discretized in N cells Ω_i such that $v(i)$ is the set of cells neighboring the cell Ω_i by the edges, $|\Omega_i|$ is the area of the cell Ω_i, $|\Gamma_{ij}|$ is the length of the edge common to the cells Ω_i and Ω_j and $\boldsymbol{n}_{ij}$ is the unit vector normal to Ω_i (see Fig. 2). The mass centers $\mathbf{x}_i$ of cell Ω_i is defined as

$$\mathbf{x}_i = \frac{1}{|\Omega_i|} \int_{\Omega_i} \mathbf{x} \mathrm{d}\mathbf{x}. \tag{2.12}$$

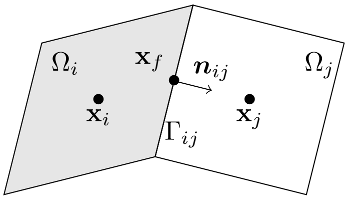

Figure 2: Notations associated with the unstructured mesh.

The time is discretized by $t^n = n\Delta t$ for $n \in \mathbb{N}$, where $\Delta t > 0$ is the time step. In the finite volume approach that is used, the notation ϕ_i^n is an approximation of

$$\frac{1}{|\Omega_i|} \int_{\Omega_i} \phi(\mathbf{x}, t^n) \mathrm{d}\mathbf{x},$$

for any quantity $\phi(\mathbf{x}, t)$.

In the sequel, the first order in space and time scheme is described.

2.3.1. Acoustic step

An approximate four-state Riemann solver [21], or the Lagrangian scheme EUCCLHYD [34] can be used to solve this system. The numerical scheme for the acoustic step reads

$$\boldsymbol{V}^\dagger = \boldsymbol{V}^n - \frac{\Delta t}{|\Omega_{\boldsymbol{i}}|} \vartheta_{\boldsymbol{i}}^n \sum_{\boldsymbol{j} \in v(\boldsymbol{i})} |\Gamma_{\boldsymbol{ij}}| \, \boldsymbol{G}_{\boldsymbol{ij}}^{\#}, \tag{2.13}$$

where $\boldsymbol{G}_{\boldsymbol{ij}}^{\#} = (-\bar{u}_{\boldsymbol{ij}}, 0, \bar{p}_{\boldsymbol{ij}} \boldsymbol{n}_{\boldsymbol{ij}}, \bar{p}_{\boldsymbol{ij}} \bar{u}_{\boldsymbol{ij}}, 0)^{\#}$ is the numerical flux and $\dagger$ corresponds to the intermediate state between the acoustic step and the transport step. The scheme can be explicit by taking $\# = n$ or implicit with $\# = \dagger$. For the approximate four-state Riemann solver of Gallice [21], the flux reads

$$\begin{aligned} \bar{u}_{\boldsymbol{ij}} &= \frac{\bar{C}_{\boldsymbol{ij}}^- \boldsymbol{u}_{\boldsymbol{i}} + \bar{C}_{\boldsymbol{ij}}^+ \boldsymbol{u}_{\boldsymbol{j}}}{\bar{C}_{\boldsymbol{ij}}^- + \bar{C}_{\boldsymbol{ij}}^+} \cdot \boldsymbol{n}_{\boldsymbol{ij}} - \frac{p_{\boldsymbol{j}} - p_{\boldsymbol{i}}}{\bar{C}_{\boldsymbol{ij}}^- + \bar{C}_{\boldsymbol{ij}}^+}, \\ \bar{p}_{\boldsymbol{ij}} &= \frac{\bar{C}_{\boldsymbol{ij}}^+ p_{\boldsymbol{i}} + \bar{C}_{\boldsymbol{ij}}^- p_{\boldsymbol{j}}}{\bar{C}_{\boldsymbol{ij}}^- + \bar{C}_{\boldsymbol{ij}}^+} - \bar{C}_{\boldsymbol{ij}}^- \bar{C}_{\boldsymbol{ij}}^+ \frac{\boldsymbol{u}_{\boldsymbol{j}} - \boldsymbol{u}_{\boldsymbol{i}}}{\bar{C}_{\boldsymbol{ij}}^- + \bar{C}_{\boldsymbol{ij}}^+} \cdot \boldsymbol{n}_{\boldsymbol{ij}} \end{aligned} \tag{2.14}$$

where $\bar{C}_{\boldsymbol{ij}}^-$ and $\bar{C}_{\boldsymbol{ij}}^+$ are the Riemann solver slopes. The choice of slopes is crucial to guarantee the positivity of the intermediate states of the Riemann solver and thus of the associated Godunov type scheme [21] (see also [12]). Their computation is detailed in [40]. In the explicit case, the Courant-Friedrichs-Lewy (CFL) condition ensures that no wave cross within the same cell. It is given by

$$\Delta t \max_{1 \le i \le N} \left[\frac{\vartheta_i}{|\Omega_i|} \max_{j \in v(i)} \left(|\Gamma_{ij}| \bar{C}_{ij} \right) \right] < \frac{1}{2}. \tag{2.15}$$

When the two phases have large pressure or density ratios, the CFL (2.15) related to the acoustic system can be very constraining. This is the case for liquid/gas interactions. Thus, the acoustic step is solved with an implicit time-scheme [10, 11, 40]. This approach is extensively detailed in [40]. We will recall here the main ideas. For the sake of simplicity, a one-dimensional problem is considered. The extension in dimension 2 follows the same lines. The speed of sound and the Riemann solver slopes are frozen at time n. Since the numerical flux $\boldsymbol{G}_{\boldsymbol{ij}}$ depends only on the velocity and the pressure, we solve the following subsystem

$$\left\{ \begin{aligned} \partial_t p + {} & a^2 \vartheta \partial_x u = 0, \\ \partial_t u + {} & \vartheta \partial_x p \quad = 0, \end{aligned} \right. \tag{2.16}$$

where $a = \rho c$ is the Lagrangian sound speed. We now look for the solution of the system

$$\boldsymbol{X}^\dagger - \boldsymbol{X}^n + \frac{\Delta t}{\Delta x} \vartheta^n [[\boldsymbol{H}]] = 0, \tag{2.17}$$

where $\boldsymbol{X} = (p_i, u_i)$ and

$$[[\boldsymbol{H}]] = (a_i^2 (\bar{u}_{i+1/2}^\dagger - \bar{u}_{i-1/2}^\dagger), \bar{p}_{i+1/2}^\dagger - \bar{p}_{i-1/2}^\dagger), \tag{2.18}$$

are the jumps of the numerical flux, computed with (2.14). Since the system (2.16) is linear in (p, u), it can be rewritten as

$$\boldsymbol{X}^\dagger - \boldsymbol{X}^n + \frac{\Delta t}{\Delta x} \boldsymbol{M} \boldsymbol{X}^\dagger = 0, \tag{2.19}$$

where $\boldsymbol{M}\boldsymbol{X} = \vartheta^n [[\boldsymbol{H}]]$. The matrix $\boldsymbol{M}$ depends on the choice made to evaluate the flux. It is given in [40] for the four-state Riemann solver of [21]. Basically, it depends on the Riemann solver slope and the sound speed. In practice, the system obtained is solved under the delta-form

$$\left(\mathsf{I_d} + \frac{\Delta t}{\Delta x} \boldsymbol{M} \right) (\boldsymbol{X}^\dagger - \boldsymbol{X}^n) = -\frac{\Delta t}{\Delta x} \boldsymbol{M} \boldsymbol{X}^n. \tag{2.20}$$

The resolution of this linear system then gives a new velocity and a prediction of the pressure. These pressure predictions are used to evaluate the numerical flux $\boldsymbol{G}_{\boldsymbol{ij}}^\dagger$ and update the acoustic variables $\vartheta^\dagger$ and $E^\dagger$ explicitly with formulae (2.13). The real pressure is then determined by the EOS (2.5). It does not seem possible to prove that the pressure obtained at the end of the acoustic step is close to the pressure given by the EOS.

2.3.2. Transport step

The transport system is resolved under the equivalent form

$$\partial_t \psi + \nabla \cdot (\boldsymbol{u} \psi) - \psi \nabla \cdot \boldsymbol{u} = 0, \tag{2.21}$$

where ψ corresponds to the variables $(\rho, \rho y, \rho \boldsymbol{u}, \rho E, z)$ of the system (2.11). The transport equation (2.21) consists of a first conservative term $\nabla \cdot (\boldsymbol{u}\psi)$ followed by a second non-conservative term $\psi \nabla \cdot \boldsymbol{u}$.

The first-order numerical scheme of the transport step is as follows

$$\psi_{\boldsymbol{i}}^{n+1} = \psi_{\boldsymbol{i}}^{\dagger} - \frac{\Delta t}{|\Omega_{\boldsymbol{i}}|} \sum_{\boldsymbol{j} \in v(\boldsymbol{i})} |\Gamma_{\boldsymbol{ij}}| \, \psi_{\boldsymbol{ij}}^{\dagger} \mathrm{u}_{\boldsymbol{ij}} + \psi_{\boldsymbol{i}}^{\dagger} \frac{\Delta t}{|\Omega_{\boldsymbol{i}}|} \sum_{\boldsymbol{j} \in v(\boldsymbol{i})} |\Gamma_{\boldsymbol{ij}}| \, \mathrm{u}_{\boldsymbol{ij}}. \tag{2.22}$$

It is solved with an explicit time scheme. The most natural choice is to use the upwind scheme to solve the conservative term. A judicious choice on the material velocity $\mathrm{u}_{\boldsymbol{ij}}$ gives a globally conservative scheme. This choice consists in taking the opposite of the first component of the acoustic flux [40]. In the case of the Gallice's Riemann solver [21], we have $\mathrm{u}_{\boldsymbol{ij}} = \bar{u}_{\boldsymbol{ij}}^{\#}$. The transport step is stable under the following CFL condition

$$\Delta t \max_{1 \le i \le N} \left[\frac{1}{|\Omega_i|} \sum_{\boldsymbol{j} \in v(\boldsymbol{i})} |\Gamma_{\boldsymbol{ij}}| \, |\mathrm{u}_{\boldsymbol{ij}}| \right] < 1. \tag{2.23}$$

2.3.3. Global scheme

The overall algorithm for a time step between t^n and t^{n+1} reads

Step 1: From a state $(\rho, \rho y, \rho \boldsymbol{u}, \rho \varepsilon, z)^n$, compute $(\rho, \rho y, \rho \boldsymbol{u}, \rho \varepsilon, z)^{\dagger}$, the approximation of the acoustic system (2.13).

Step 2: Find the fluid state $(\rho, \rho y, \rho \boldsymbol{u}, \rho \varepsilon, z)^{n+1}$ by solving the transport system (2.11) with the initial state $(\rho, \rho y, \rho \boldsymbol{u}, \rho \varepsilon, z)^{\dagger}$.

The global scheme reads

$$\left\{ \begin{array}{lcll}
\rho_{\boldsymbol{i}}^{n+1} & = & \rho_{\boldsymbol{i}}^{n} & - \dfrac{\Delta t}{|\Omega_{\boldsymbol{i}}|} \displaystyle\sum_{\boldsymbol{j} \in v(\boldsymbol{i})} |\Gamma_{\boldsymbol{ij}}| \, \rho_{\boldsymbol{ij}}^{\dagger} \bar{u}_{\boldsymbol{ij}}^{\#}, \\
(\rho y)_{\boldsymbol{i}}^{n+1} & = & (\rho y)_{\boldsymbol{i}}^{n} & - \dfrac{\Delta t}{|\Omega_{\boldsymbol{i}}|} \displaystyle\sum_{\boldsymbol{j} \in v(\boldsymbol{i})} |\Gamma_{\boldsymbol{ij}}| \, (\rho y)_{\boldsymbol{ij}}^{\dagger} \bar{u}_{\boldsymbol{ij}}^{\#}, \\
(\rho \boldsymbol{u})_{\boldsymbol{i}}^{n+1} & = & (\rho \boldsymbol{u})_{\boldsymbol{i}}^{n} & - \dfrac{\Delta t}{|\Omega_{\boldsymbol{i}}|} \displaystyle\sum_{\boldsymbol{j} \in v(\boldsymbol{i})} |\Gamma_{\boldsymbol{ij}}| \Big((\rho \boldsymbol{u})_{\boldsymbol{ij}}^{\dagger} \bar{u}_{\boldsymbol{ij}}^{\#} + \bar{p}_{\boldsymbol{ij}}^{\#} \Big), \\
(\rho E)_{\boldsymbol{i}}^{n+1} & = & (\rho E)_{\boldsymbol{i}}^{n} & - \dfrac{\Delta t}{|\Omega_{\boldsymbol{i}}|} \displaystyle\sum_{\boldsymbol{j} \in v(\boldsymbol{i})} |\Gamma_{\boldsymbol{ij}}| \Big((\rho E)_{\boldsymbol{ij}}^{\dagger} \bar{u}_{\boldsymbol{ij}}^{\#} + \bar{p}_{\boldsymbol{ij}}^{\#} \bar{u}_{\boldsymbol{ij}}^{\#} \Big), \\
z_{\boldsymbol{i}}^{n+1} & = & z_{\boldsymbol{i}}^{n} & - \dfrac{\Delta t}{|\Omega_{\boldsymbol{i}}|} \displaystyle\sum_{\boldsymbol{j} \in v(\boldsymbol{i})} |\Gamma_{\boldsymbol{ij}}| \, z_{\boldsymbol{ij}}^{n} \bar{u}_{\boldsymbol{ij}}^{\#} + z_{\boldsymbol{i}}^{n} \dfrac{\Delta t}{|\Omega_{\boldsymbol{i}}|} \displaystyle\sum_{\boldsymbol{j} \in v(\boldsymbol{i})} |\Gamma_{\boldsymbol{ij}}| \, \bar{u}_{\boldsymbol{ij}}^{\#}.
\end{array} \right. \tag{2.24}$$

This scheme is clearly conservative for the densities, momentum, and total energy equations. It preserves the contact discontinuities, namely constant $\boldsymbol{u}$ and p states.

Remark 2
Numerical flux depends on Δt. Indeed, the variables of the flux with the exponent $\dagger$ are updated by the acoustic step (2.13) which depends on the time step. Thus, stationary solutions depend on the time step. We can see the two steps as an implicit method to calculate the numerical flux associated with (2.24).

3. Second-order extension

3.1. Second-order in space extension

When using diffuse interface methods, the volume fraction will naturally be diffused at the interface between the two fluids considered. The simple first-order in space scheme used in both the acoustic and the transport step will produce a numerical diffusion of the solution that is far too large to accurately follow the interface. To overcome this problem, we use a second-order MUSCL-type method [32] called U-MUSCL [8]. It consists in using in the numerical flux the polynomial reconstructions $\hat{\alpha}_{ij}$ and $\hat{\alpha}_{ji}$ of the solution on Γ_{ij} such that

$$\begin{aligned}
\hat{\alpha}_{ij} &= \alpha_i + \frac{\kappa}{2}(\alpha_j - \alpha_i) + (1-\kappa)\boldsymbol{\nabla}\alpha_i.(\mathbf{x}_f - \mathbf{x}_i), \\
\hat{\alpha}_{ji} &= \alpha_j + \frac{\kappa}{2}(\alpha_i - \alpha_j) + (1-\kappa)\boldsymbol{\nabla}\alpha_j.(\mathbf{x}_f - \mathbf{x}_j),
\end{aligned} \tag{3.1}$$

with $\kappa \in [-1, 1]$ a parameter. The use of the mass center $\mathbf{x}_i$ given by (2.12), instead of any point in cell Ω_i, ensures that the reconstructions $\hat{\alpha}_i^n$ of variable α_i^n are conservative, i.e.

$$\frac{1}{|\Omega_i|} \int_{\Omega_i} \hat{\alpha}_i^n(\mathbf{x}) \mathrm{d}\mathbf{x} = \alpha_i^n. \tag{3.2}$$

By writing (3.1) it in the form

$$\hat{\alpha}_{ij} = \kappa \frac{(\alpha_j + \alpha_i)}{2} + (1-\kappa)\left(\alpha_i + \boldsymbol{\nabla}\alpha_i.(\mathbf{x}_f - \mathbf{x}_i)\right), \tag{3.3}$$

it can be seen as a combination of the linear interpolation (first term) and the linear extrapolation (second term) of

$\hat{\alpha}_{ij}$. It is an extension of van Leer's κ-scheme on unstructured grids. Note that $\kappa = 0$ returns the conventional MUSCL reconstruction. As shown in [37], the U-MUSCL scheme with $\kappa = 1/3$ gives more accurate results than $\kappa = 0$. However, this method is second-order only if the center of the face $\mathbf{x}_f$ lies exactly between the mass centers of cells $\mathbf{x}_i$ and $\mathbf{x}_j$ (see Fig. 2). Therefore, a modification from [37] must be employed to preserve the second-order accuracy. This consists in modifying the reconstruction (3.1) such that

$$\hat{\alpha}_{ij} = \alpha_i + \frac{\kappa}{2}(\alpha_p - \alpha_i) + (1-\kappa)\boldsymbol{\nabla}\alpha_i.(\mathbf{x}_f - \mathbf{x}_i), \qquad (3.4)$$

where

$$\alpha_p = \alpha_j + \boldsymbol{\nabla}\alpha_j.(2\mathbf{x}_f - \mathbf{x}_i - \mathbf{x}_j). \qquad (3.5)$$

The U-MUSCL scheme (3.4) with the second-order preserving modification will be used as the reconstruction method due to its simplicity and accuracy when using $\kappa = 1/3$. As shown in [39], U-MUSCL with $\kappa = 1/3$ can be third-order accurate in cell-averaged solutions on regular grids for one-dimensional problem, and in the point-valued solution on regular grids for linear equations in all dimensions. However, only second-order can be obtained in our configuration, namely the two-dimensional case on unstructured grid.

3.1.1. Gradient computation on unstructured meshes

The MUSCL-type scheme presented previously requires the computation of the gradient of the unknowns on unstructured meshes. There are two methods main for gradient computation: the Green-Gauss method (GG) and the Least SQuares method (LSQ). The first one is based on the application of the Green-Ostrogradski theorem. Although easy to implement and inexpensive, it is not very accurate on deformed meshes [49]. Thus, the LSQ method is preferred here for its robustness and accuracy. It is based on the Taylor development of the solution within a cell i on a stencil $v(i)$ composed of its neighbors. It can be composed of neighbors per edge, neighbors per vertex, or from an even more extended stencil. These first two configurations are represented in Fig. 3. An enlarged stencil for gradient computation enables greater accuracy, especially when the mesh is highly distorted.

The LSQ method consists in solving an over-determined system $AX = b$ where $X = \boldsymbol{\nabla}\alpha_i$ (see Appendix A). By construction, the method is exact for any linear function, regardless of the mesh. This is essential to obtain second-order accuracy with MUSCL-type schemes. The accuracy of the gradient computation can be improved by using a weighted matrix W, usually diagonal, with coefficients ω_{kk} such as

$$\omega_{kk} = ||\mathbf{x}_{j_k} - \mathbf{x}_i||^{-q}, \qquad (3.6)$$

where q is a positive parameter. When $q = 0$, we find the unweighted method. With $q = 1$, the weight corresponds to the inverse of the distance between the mass center of cell i and cell j. In this work, q is set to $3/2$ [49]. We thus need to resolve $WAX = Wb$. This over-determined system is solved by going through the normal equations, i.e., by multiplying the system by $(WA)^T$, and the solution reads

$$X = (A^TW^TWA)^{-1}A^TW^TWb. \qquad (3.7)$$

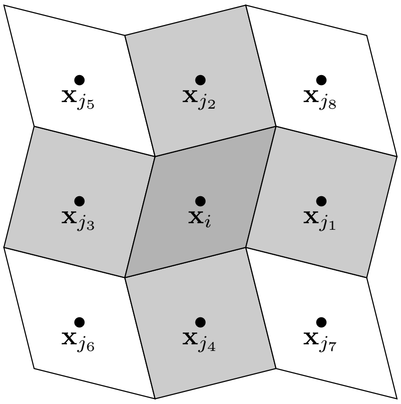

Figure 3: Schematic representation of the neighborhood by edge (gray) and the neighborhood by vertex (white and gray) for the calculation of the gradient on cell i by the LSQ method.

In the case where the matrix is ill-conditioned however, the gradient calculation could be imprecise. Another approach to avoid such a problem is to use the QR decomposition. The matrix WA can be decomposed as $WA = QR$ where Q is an orthogonal matrix and R is an upper triangular matrix. The solution is then written

$$X = R^{-1}Q^TWb. \qquad (3.8)$$

The second method is thus preferred. The QR decomposition is performed with the modified Gram-Schmidt algorithm [22]. Note that the matrix $R^{-1}Q^TW$ consists only of geometrical parameters. When the mesh is not moving, it is then sufficient to calculate it once when initializing the calculations and to store it. This method can give second-order accurate gradient reconstruction for smooth curvilinear mesh or on meshes of identical parallelograms [49].

3.1.2. Gradient limiter

In order to eliminate oscillations inherent to high-order schemes and capture discontinuities, these reconstructions are limited by a function of the local gradient, called “limiter”. Many limiters exist in the literature, designed to have different properties. In the case of the five-equation system, the volume fraction is a discontinuous variable, which follows a transport equation. Following the lines of [42, 7, 15], the idea here is to apply a compressive limiter to this variable, which allows a better representation of the interface between the two fluids. For the other variables, namely densities, velocity and pressure, the limiter should be as robust as possible, given the implicit treatment of the acoustic step.

The reconstruction $\hat{\alpha}^n_{ij}$ is rewritten in the form

$$\hat{\alpha}_{ij} = \alpha_i + \phi_i\Delta\alpha_{i,j}, \qquad (3.9)$$

where ϕ_i is the gradient limiter, and

$$\Delta\alpha_{i,j} = \frac{\kappa}{2}\left(\alpha_p - \alpha_i\right) + (1-\kappa)\boldsymbol{\nabla}\alpha_i.(\mathbf{x}_f - \mathbf{x}_i). \tag{3.10}$$

Proposition 1

Let ϕ_i the limiter of the reconstruction of α_i in cell i, such that

$$\phi_i = \begin{cases} \min\left(\beta, \dfrac{\alpha_i - \alpha_i^{\min}}{|\Delta\alpha_i|^{\max}}, \dfrac{\alpha_i^{\max} - \alpha_i}{|\Delta\alpha_i|^{\max}}\right) & \textit{if } |\Delta\alpha_i|^{\max} \neq 0, \\ 0 & \textit{otherwise.} \end{cases} \tag{3.11}$$

with $|\Delta\alpha_i|^{max} = \max_{j\in v(i)}|\Delta\alpha_{i,j}|$, $\alpha_i^{\min} = \min_{j\in v(i)}(\alpha_i, \bar{\alpha}_j)$ *and* $\alpha_i^{\max} = \max_{j\in v(i)}(\alpha_i, \bar{\alpha}_j)$. *Depending on the parameters β and $\bar{\alpha}_j$, this limiter displays different properties :*

- *If $\beta = 1$ and $\bar{\alpha}_j = \dfrac{\alpha_i\omega_i + \alpha_j\omega_j}{\omega_i + \omega_j}$ with $\omega_i = ||\mathbf{x}_{j_k} - \mathbf{x}_i||^{-1}$ then the limiter is monotonicity preserving, i.e.*

$$\forall j \in v(i),\ \alpha_i \leq \alpha_j \implies \hat{\alpha}_{ij} \leq \hat{\alpha}_{ji}. \tag{3.12}$$

- *If $\beta > 1$ and $\bar{\alpha}_j = \alpha_j$, the limiter is compressive.*

Proof. The design of the previous limiter is provided in Appendix B. ☐

This approach is used in [42] in the framework of one-dimensional limiter for two-phase flows, where the compressive limiter is used on the density whereas the minmod limiter is used on the velocity and the pressure. In [7], a similar β-limiter is designed without the monotonicity preserving condition. The compressive limiter (3.11) with $\beta = 2$ is used on the volume fraction of a two–phase model while the less compressive limiter with $\beta = 1$ is used on the others variables. In the work presented in [15], a family of β-limiters is designed from the approach of [5] where as previously, the compressive limiter is used on the volume fraction only.

Monotonicity preserving. When dealing with large pressure or density ratio, as in the study of liquid-gas interaction, the monotonicity preserving property can be essential, in order to improve robustness. The well-known minmod limiter verifies this condition, which explains why it is very popular in industrial codes.

Compressive property. The compressive nature of a method or limiter reflects the ability to accurately reproduce a discontinuity. For example, the superbee limiter [50] is well-known to sharpen sinusoidal profiles and to behave well on discontinuity transport. This property is particularly valuable in the context of immiscible fluid flows, as it improves the representation of the interface between these two fluids [42, 7, 15]. When the limiter (3.11) is allowed to take values greater than 1, it is then compressive.

Remark 3

When a second-order in space scheme is used, the maximum time step given by CFL conditions (2.15) and (2.23) must be divided by two (see [6] for example).

3.1.3. Second-order in space scheme in the splitting strategy

The limiter (3.11) is used in the context of the five-equation system, while reconstructions are performed with the U-MUSCL scheme with $\kappa = 1/3$. The objective is to sharpen the fluid's discontinuities by reducing the number of mixture cells. The reconstructed variables are the primitive variables, in order to limit velocity and pressure oscillations. They are reconstructed as follows

Acoustic step: $(\boldsymbol{u}, p)^n$ are reconstructed with $\beta = 1$.

Transport step: $(\rho_1, \rho_2, \boldsymbol{u}, p)^\#$ are reconstructed with $\beta = 1$ and $z^\#$ with $\beta = 2$. The conservative variables are deduced from the primitive ones with

$$\begin{cases} \rho &= z\rho_1 + (1-z)\rho_2, \\ \rho y &= z\rho_1, \\ \rho\boldsymbol{u} &= \left(z\rho_1 + (1-z)\rho_2\right)\boldsymbol{u}, \\ \rho\varepsilon &= \sum_k z_k\rho_k\varepsilon_k = \sum_k z_k \dfrac{p + \gamma_k\pi_k}{\gamma_k - 1}, \\ \rho E &= \rho\varepsilon + \dfrac{1}{2}\rho\boldsymbol{u}\cdot\boldsymbol{u}. \end{cases} \tag{3.13}$$

Remark 4

The limiter needs the computation of α_i^{min} and α_i^{max}, the local extrema. The 5-point stencil, i.e., with the edges neighbors, is used for the acoustic step, while the 9-point stencil i.e., with the vertex neighbors is utilized for the transport step (see Fig. 3). Better convergence properties have been observed numerically on the acoustic step with only 5 points.

3.2. Time-scheme

3.2.1. The Heun method

The time scheme is important to increase the accuracy of the overall scheme, especially when high-order in space schemes are used. This prevents the appearance of numerical artifacts that will degrade the solution, as shown in [16] for instance. To this end, we could use the Heun method also called Runge-Kutta TVD, which we apply on the global scheme (2.24). It reads

$$\begin{aligned} \mathbf{U}^* &= \mathbf{U}^n + \Delta t\mathbb{F}(\mathbf{U}^n, \Delta t), \\ \mathbf{U}^{**} &= \mathbf{U}^* + \Delta t\mathbb{F}(\mathbf{U}^*, \Delta t), \\ \mathbf{U}^{n+1} &= \frac{1}{2}\left(\mathbf{U}^n + \mathbf{U}^{**}\right), \end{aligned} \tag{3.14}$$

with $\mathbf{U}$ being the conservative variables $(\rho, \rho y, \rho\boldsymbol{u}, \rho\varepsilon, z)$ and $\mathbb{F}$ is a numerical flux discretized in (2.24). It is not clear that this scheme is second-order in the case of the splitting strategy because of the time step dependence of the numerical flux (see Rem. 2). Indeed, the numerical flux is a first-order in time approximation of the spatial operator. However, it does improve the numerical solution, which will be shown in the results section.

3.2.2. An alternative implicit time-scheme

The scheme described above is simple to implement and robust. When an implicit approach is used in the acoustic step however, it must be repeated twice per time step, which induces a significant cost in computation time. For this, a new implicit scheme based on the Crank-Nicolson scheme has been developed. The modified scheme proposed here reads

$$\frac{\boldsymbol{V}^{\dagger} - \boldsymbol{V}^{n}}{\Delta t} = -\frac{1}{2}\vartheta^{n}\left(\nabla \cdot \boldsymbol{G}(\boldsymbol{V}^{\dagger}) + \nabla \cdot \boldsymbol{G}(\boldsymbol{V}^{n})\right). \tag{3.15}$$

This scheme is not the Crank-Nicolson scheme because it is not second-order since we kept ϑ^n for the explicit and implicit terms. It can be seen as the average of the flux given by the explicit (2.13) and the implicit (2.13) versions of the acoustic step. The truncation error of this modified Crank-Nicolson scheme is smaller than that of the first implicit scheme (see Appendix C). The numerical scheme for the acoustic step reads

$$\boldsymbol{V}^{\dagger} = \boldsymbol{V}^{n} - \frac{\Delta t}{|\Omega_{\boldsymbol{i}}|}\vartheta_{\boldsymbol{i}}^{n} \sum_{\boldsymbol{j}\in\upsilon(\boldsymbol{i})} |\Gamma_{\boldsymbol{ij}}| \, \frac{1}{2}\left(\boldsymbol{G}_{\boldsymbol{ij}}^{n} + \boldsymbol{G}_{\boldsymbol{ij}}^{\dagger}\right). \tag{3.16}$$

The resolution of (3.16) follows the same line as the first-order implicit time scheme. In the one-dimensional case, it is easy to show that the new scheme leads to solve under the delta-form the system

$$\left(\mathsf{I_d} + \frac{\Delta t}{2\Delta x}\boldsymbol{M}\right)\left(\boldsymbol{X}^{\dagger} - \boldsymbol{X}^{n}\right) = -\frac{\Delta t}{\Delta x}\boldsymbol{M}\boldsymbol{X}^{n}. \tag{3.17}$$

From an implementation point of view, this represents a small modification of the velocity-pressure system (2.16) resolution algorithm. Once again, the other equations are solved explicitly. In order to have a globally conservative scheme, the material velocity used in the transport step must read

$$\mathfrak{u}_{\boldsymbol{ij}} = \frac{\bar{u}_{\boldsymbol{ij}}^{n} + \bar{u}_{\boldsymbol{ij}}^{\dagger}}{2}. \tag{3.18}$$

This comes from the same arguments used in [10, 40] in order to have a globally conservative scheme.

3.2.3. Extension with the second-order in space scheme

When using the second-order scheme in space, nonlinearities introduced by the limiter make it impossible to write the flux jump as a matrix-vector product of $\boldsymbol{X}$. A conventional way to solve non-linear equations is to use a quasi-Newton method. Using this method, the solution is obtained by iterating over the following equation

$$\left(\mathsf{I_d} + \frac{\Delta t}{\Delta x}\boldsymbol{M}\right)\left(\boldsymbol{X}^{k+1} - \boldsymbol{X}^{k}\right) = -\boldsymbol{X}^{k} + \boldsymbol{X}^{n} - \frac{\Delta t}{\Delta x}\vartheta^{n}[[\boldsymbol{H}^{k}]], \tag{3.19}$$

with $k = 0, ..., \infty$. The matrix $\boldsymbol{M}$ is built with the first-order flux while the right-hand side of (3.19) is computed with the second order flux. Note that a single iteration over (3.19) gives exactly (2.20), the system solved when first-order in space scheme is used. Through this method, the implicit time scheme converges to the second-order in space solution. When using the second implicit scheme, equation (3.19) becomes

$$\left(\mathsf{I_d} + \frac{\Delta t}{2\Delta x}\boldsymbol{M}\right)\left(\boldsymbol{X}^{k+1} - \boldsymbol{X}^{k}\right) = -\boldsymbol{X}^{k} + \boldsymbol{X}^{n} - \frac{\Delta t}{2\Delta x}\vartheta^{n}\left([[\boldsymbol{H}^{k}]] + [[\boldsymbol{H}^{n}]]\right). \tag{3.20}$$

Remark 5
In practice, we use a convergence threshold ϵ set to 10^{-5} with a maximum of 10 iterations. These values have proven to be sufficient in the simulations performed.

4. Numerical results

In this section, a selection of numerical results for the one and two-dimensional cases are presented. The first cases will illustrate the accuracy of the compressive limiter ($\beta = 2$) on the classical pure transport equation. The RK2-TVD time scheme presented in the previous section is always used for pure transport cases.

The next cases will show the ability of the second-order method to simulate complex two-phase flows. We denote by EXEX the explicit scheme for both the acoustic and transport steps, while IMEX is the implicit-explicit strategy of the splitting scheme. When adding RK2, the RK2-TVD scheme is thus used on the overall algorithm. The CNEX scheme denotes the new implicit-explicit scheme built from a modification of the Crank-Nicolson scheme. For two-dimensional liquid-gas or gas-gas cases, the density gradient will be computed in log scale during post-processing, as $\log(|\nabla\rho|)$, in order to reproduce numerical Schlieren.

4.1. Zalesak's disk

We consider here the classical Zalesak's disk test case [54], namely a disk with a slot rotating in the velocity field $\boldsymbol{u}(x, y) = (0.5 - y, x - 0.5)$ m.s^{-1} on the domain $\Omega = [0, 1]$ m × $[0, 1]$ m. The disk is defined at the initial time by

$$z(x, y) = \begin{cases} 1 \text{ if } \left(||\mathbf{x} - \mathbf{c}||< r\right) \text{ and} \\ \quad \left(|x - c_x|\geq e \text{ or } y - c_y > l\right), \\ 0 \text{ otherwise,} \end{cases}$$

with $\mathbf{x} = (x, y)$, $\mathbf{c} = (0.5, 0.75)$ m, $r = 0.15$ m, $e = 0.025$ m and $l = 0.1$ m. The CFL is set to 0.4 and 256×256 cells are used with constant boundary conditions. The results in Fig. 4 are obtained after one revolution at the final time $t_f = 2\pi s$.

The present limiter gives very good results. The interface is very sharp and the shape of the disk is well-preserved, almost symmetrical. The use of $\kappa = 1/3$ (see Fig. 4.a) gives a good resolution of the slot and the corners, compared to the conventional MUSCL method with $\kappa = 0$ (see Fig. 4.b). This might be because the method with $\kappa = 1/3$ is third-order accurate on the transport equation on Cartesian mesh.

4.2. Kothe-Rider advection

We now consider the Kothe-Rider forward-backward advection test case [43] on the domain $\Omega = [0, 1]$ m $\times$ $[0, 1]$ m. This test case consists in transport a circle in a backward-forward velocity field such that

$$\boldsymbol{u}(x, y, t) = \begin{pmatrix} -\sin(\pi y)\cos(\pi y)\sin(\pi x)^2\cos(\pi t/t_f) \\ \sin(\pi x)\cos(\pi x)\sin(\pi y)^2\cos(\pi t/t_f) \end{pmatrix}.$$

The circle of radius $R = 0.15$ m is set at $(0.5, 0.75)$ m. The CFL is set to 0.2 and 256×256 cells are used with constants boundary conditions. The results in Fig. 5 are obtained at the intermediate time $t = 3s$ and at the final time $t_f = 6s$.

At first, until $t = 3s$, the velocity field deforms the disk into a filament. The filament obtained (see Fig. 5.a) is well-captured in regions where it is large enough regarding the cell's size. In a second time, the velocity field rewinds the filament to reform a disk. At the end, the shape of the disk is quite well-preserved (see Fig. 5.b). Some diffusion from the forward part deteriorates the results. A mesh with more cells gives a better disk resolution.

4.3. One-dimensional liquid-gas shock tube

We consider here the classical one-dimensional liquid-gas shock tube test on $\Omega = [0, 1]$ m, studied in [51] for instance. The stiffened gas EOS is used for the liquid, while the gas is modelled by the perfect gas EOS. The initial conditions read

$$(\rho, u, p, \gamma, \pi) = \begin{cases} (10^3, 0, 10^9, 4.4, 6 \times 10^8) & \text{if } x \leq 0.7 \text{ m}, \\ (5, 0, 10^5, 1.4, 0) & \text{else}. \end{cases}$$

The CFL number for the transport step is set to 0.25, and we use 400 cells with constant boundary conditions. The final time is set to $t_f = 240\mu s$. This case serves to test the accuracy of the different time schemes to represent the three waves of the problem, that are rarefaction wave, contact discontinuity and shock. This is a challenging test case, since large pressure and density ratios are involved. The results are presented in Fig. 6.

The results are in very good agreement with the exact solution. The three waves are well-represented, especially the contact discontinuity, thanks to the compressive limiter used on the volume fraction. One can see an undershoot on contact discontinuity of the density (see Fig. 6.a). This observation is quite common when sharp interface techniques are used, as the anti-diffusive scheme [30, 20]. Regarding velocity and pressure, the CNEX time scheme gives more accurate results than the IMEX scheme or the IMEX+RK2 strategy, especially near the rarefaction wave. It also reduces the overshoot on the density and better localizes the shock position.

4.4. Two-dimensional Air-R22 interaction

We shall now consider the experiment of Haas & Sturtevant [24]. In this test case, a shock wave at Mach 1.22 propagating through the air hits an R22 gas cylinder of radius $R = 25$ mm located at $(130\text{ mm}, 44.5\text{ mm})$. Many simulations of this case can be found in the literature, such as [46, 30, 26]. The computational domain $\Omega = [0, 200]$ mm $\times$ $[0, 89]$ mm is described in Fig. 7.

The initial states of both fluids in the pre- and post-shock regions are given in Tab. 1. Both fluids are modeled by perfect gas EOS with $\gamma = 1.4$ for the air and $\gamma = 1.249$ for the R22. The pre-shock density, velocity, and pressure are computed with the shock wave relation (see [50] for instance) such that the Mach shock is 1.22. Each phase is modeled by perfect gas EOS.

Location	ρ (kg.m^{-3})	$\boldsymbol{u}$ (m.s^{-1})	p (10^5Pa)
Air (shock)	1.926919	(-105.495,0)	1.5698
Air	1.4	(0,0)	1
R22	4.4154	(0,0)	1

Table 1: Two-dimensional Air-R22 interaction : initial data.

Because of the symmetry of the problem, we use a domain of $\Omega = [0, 200]$ mm $\times$ $[44.5, 89]$ mm with boundary symmetric condition at the lower side, a wall boundary condition at the upper side, an outflow boundary conditions on the left side and a supersonic inlet boundary condition on the right side. The mesh is composed of 1600×356 cells. In this case, the implicit time scheme is not useful since the ratio of densities and pressures is approximately 1. The explicit version of the time scheme is therefore used. The CFL number for both steps is set to 0.25. The final time is $t_f = 1020\mu s$.

The numerical Schlieren of this case is presented in Fig. 8. For the lower half, the results are obtained with the EXEX time-scheme, while the EXEX+RK2 strategy is used for the upper half. For both simulations, the second-order in space scheme with compressive limiter is used. When the shock impacts the R22 gas, the cylinder is deformed. This velocity difference, combined with the interaction of the interface with the transmitted shock waves produce hydrodynamic instabilities, and curling vortices are generated at the interface between the two gases. The scheme is able to reproduce a large scale and finer flow structure, while maintaining a very sharp interface

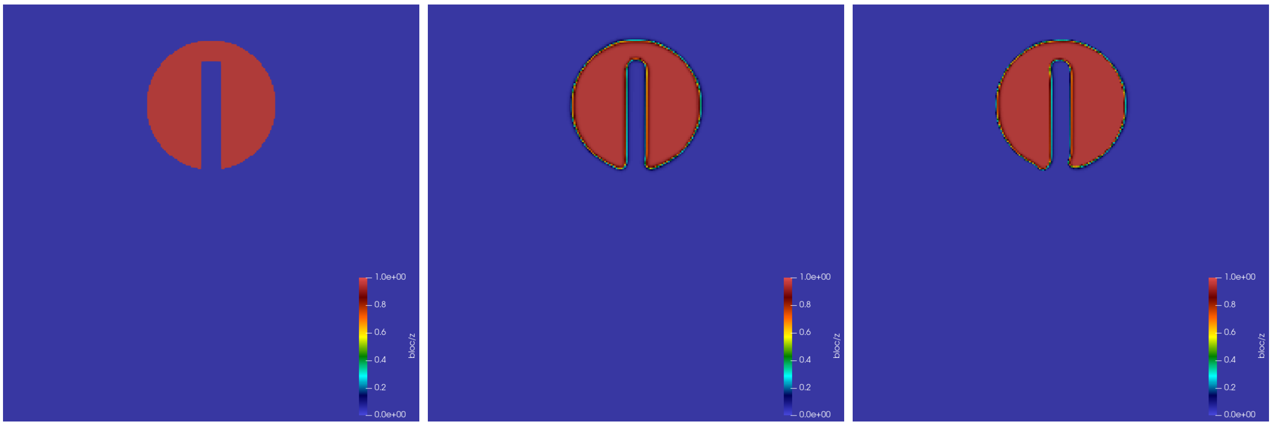

(a) (b) (c)

Figure 4: Zalesak's disk test case. Initial condition (a), solution after one rotation with $\kappa = 1/3$ (b) and with $\kappa = 0$ (c).

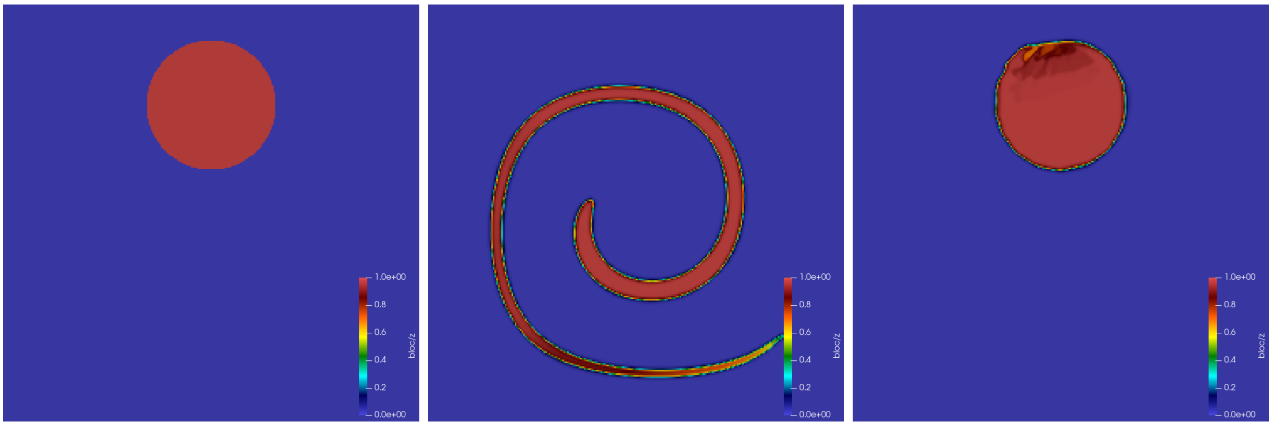

(a) (b) (c)

Figure 5: Kothe-Rider advection test case. Initial condition (a), solution obtained at the intermediate time $t = 3s$ (b) and solution at the final time $t = 6s$ (c).

throughout the simulation. The results are in good agreement with the experiments of [24] and with numerical results from the literature [30, 31, 28, 14]. The use of the EXEX-RK2 scheme appears to attenuate the spurious waves that appear with the EXEX scheme.

4.5. Two-dimensional liquid-gas interaction

We shall now consider a two-dimensional liquid-gas interaction, widely studied in the literature [44, 30, 28, 40]. The rectangular computational domain $\Omega = [0, 2]$ m $\times$ $[0, 1]$ m is described in Fig. 9. A gas cylinder of radius $R = 0.4$ m is initially at rest in a liquid at $(0.5, 0.5)$ m while a shock at $x = 0.04$ m propagates in the liquid from left to right.

The initial conditions of each phase are provided in Tab. 2. The air is modeled by perfect gas EOS with $\gamma = 1.4$ while the liquid is modeled by stiffened gas EOS with $\gamma = 4.4$ and $\pi = 6.8 \times 10^8$.

Location	ρ (kg.m^{-3})	$\boldsymbol{u}$ (m.s^{-1})	p (Pa)
Liquid (shock)	1030.9	(300,0)	3×10^9
Liquid	1000	(0,0)	10^5
Gas	1	(0,0)	10^5

Table 2: Two-dimensional liquid-gas interaction : initial data

Because of the symmetry of the problem, a domain of $\Omega = [0, 2]$ m$\times[0.5, 1]$ m is used with a boundary symmetric condition at the lower side, a wall boundary condition at the upper side and inflow/outflow boundary conditions on the other sides. The mesh is composed of 1600×400 cells. The CNEX time scheme is used with the second-order in space strategy. Since the acoustic step is implicit, the time step is computed with the transport condition (2.23) with a CFL number set to 0.25.

Volume fraction and numerical Schlieren are presented on Fig. 10. The results are in good agreement with the results presented in [44, 30, 28, 40]. The compressive limiter gives a sharp interface of the volume fraction. The propagation waves are shown on numerical Schlieren. The

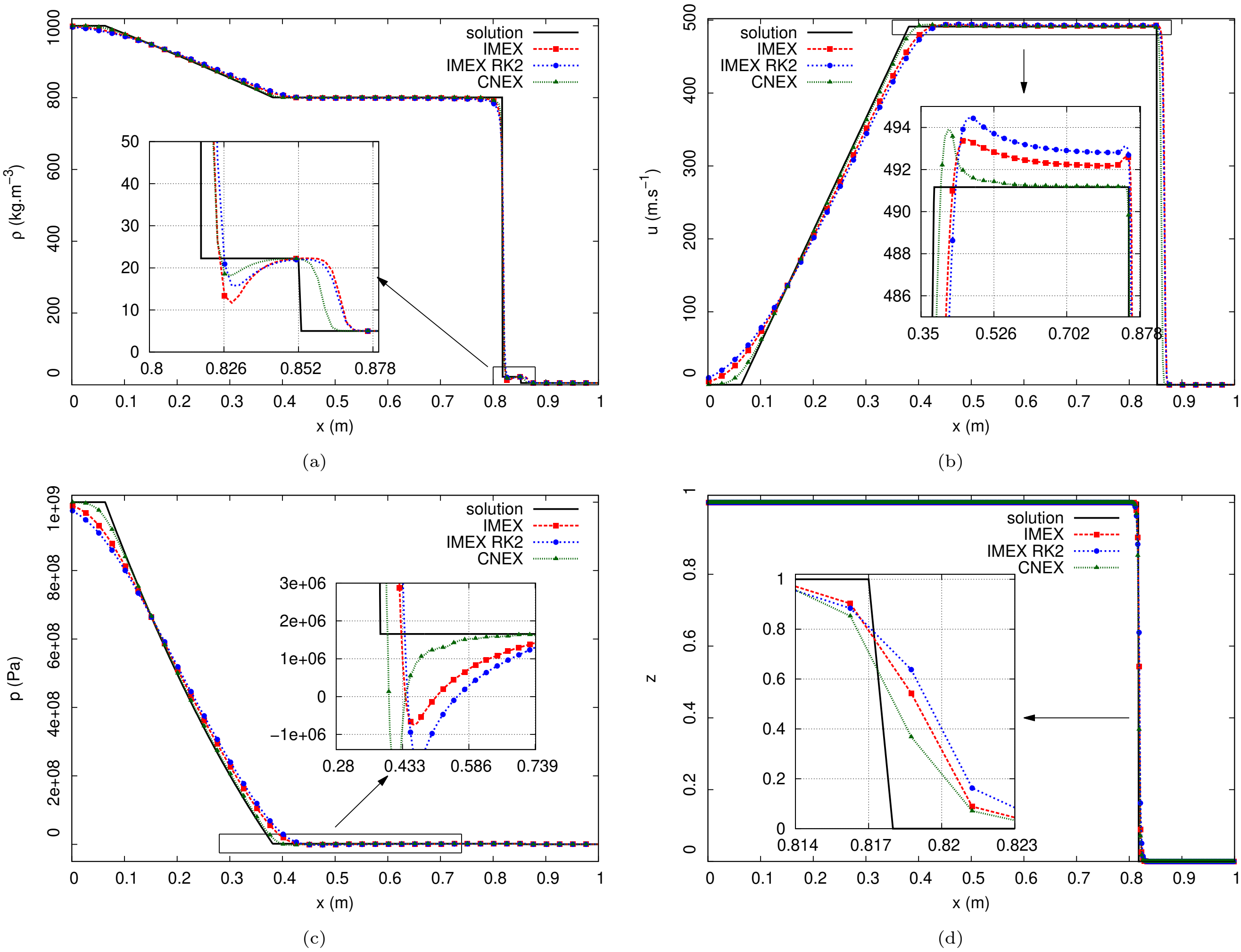

(a)

(b)

(c)

(d)

Figure 6: One-dimensional liquid-gas shock tube test case. The density (upper left), velocity (upper right), pressure (lower left) and volume fraction (lower right) are compared at the final time $t_f = 240\mu s$ with the exact solution. Except for the volume fraction, only one cell in 10 is represented by points.

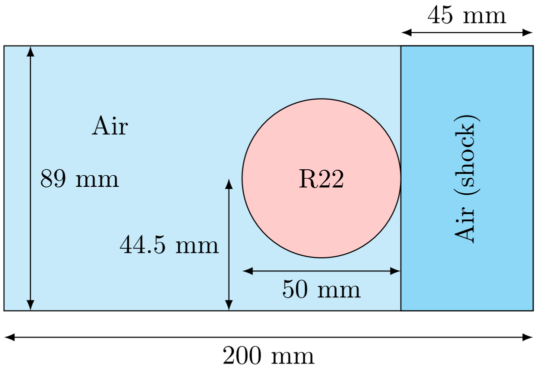

Figure 7: Two-dimensional Air-R22 interaction : geometric description of the test case.

shock wave hits the gas cylinder and compresses it while propagating inside. When the shock reaches at the left of the cylinder, the gas is split into two different cylinders.

Remark 6

Many schemes are unable to cope with this test case because of the high ratio of pressure and density, even with explicit time schemes. The robustness of the method come from the exact conditions on the Riemann solver slopes to ensure positivity of the intermediate states [40]. However, these conditions are derived from the explicit time-scheme of the acoustic step. In our case, when an implicit time-scheme is used, no conditions can be derived to guarantee that the solution remains in the convex set of admissible solutions, which ensures that the sound speed given by (2.7) is real, and the mixture density is positive. When using the compressive limiter however, it happens in this test case that $p + \pi$ becomes negative in mixture cells where the volume fraction of liquid is approximately 10^{-4} and the mixture density is about 10^{-3}. To overcome this issue, when the square of the velocity of the mixing sound speed in cell i is negative, it is calculated with

$$c_i^2 = \max(c_{i,liq}^2, c_{i,gas}^2) \tag{4.1}$$

where $c_{i,liq}$ and $c_{i,gas}$ are the sound speed of the liquid

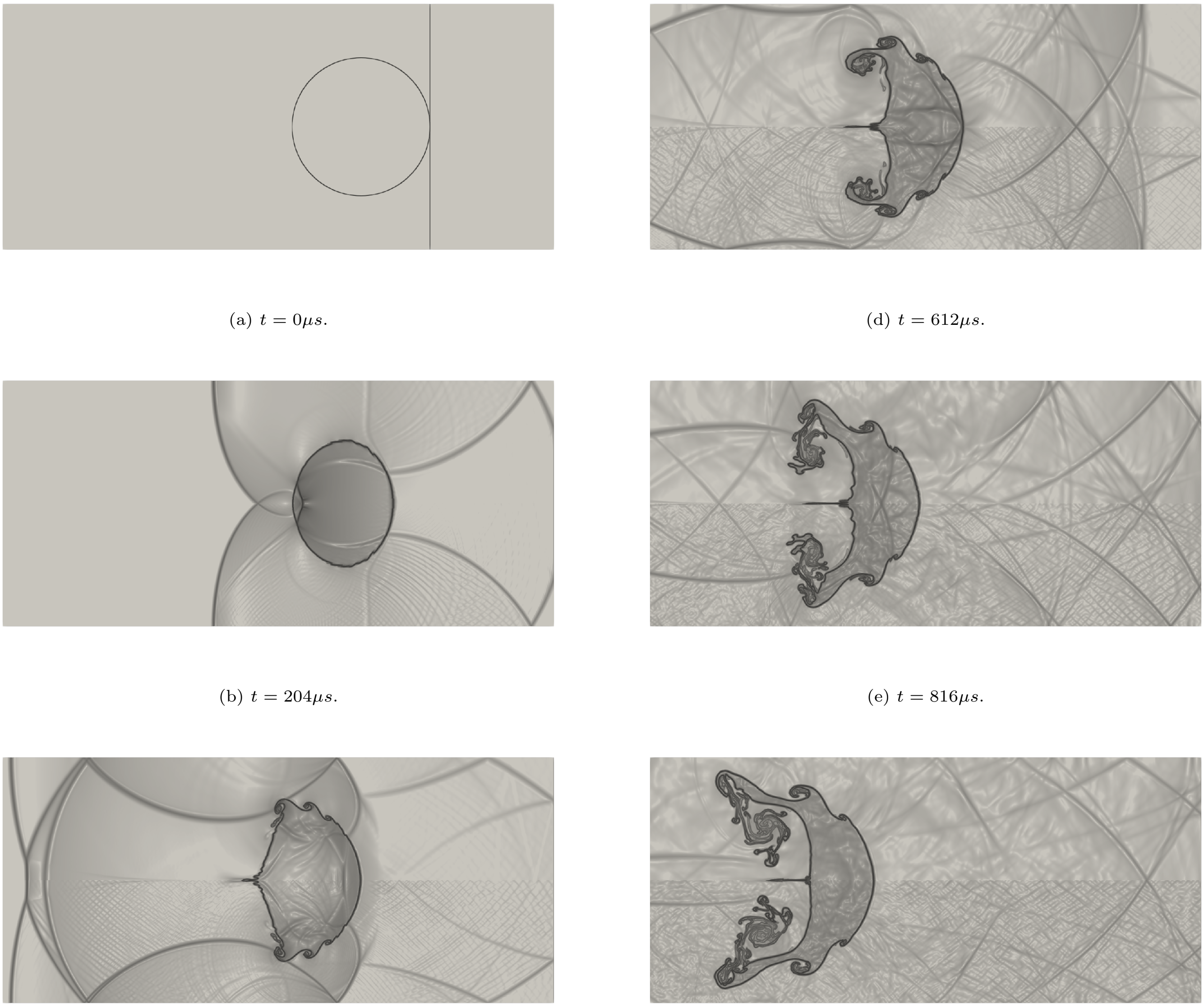

(a) $t = 0\mu s$.

(d) $t = 612\mu s$.

(b) $t = 204\mu s$.

(e) $t = 816\mu s$.

(c) $t = 408\mu s$.

(f) $t = 1020\mu s$.

Figure 8: Numerical Schlieren of the air-R22 interaction test case. Results of the EXEX scheme (lower half) and results with the EXEX+RK2 scheme (upper half) at several times.

phase and gas phase in cell i. This fix can be seen as adding diffusion to the implicit resolution of the acoustic step, where the slopes of the Riemann solver are locally increased. It is the only part where the sound speed is needed.

4.6. Two-dimensional liquid-gas interaction on deformed mesh

All the cases presented above were performed on Cartesian grids. Thus, the last liquid-gas test case is reproduced on a deformed mesh, in order to show that the method works on unstructured grids. The deformation is performed from a Cartesian mesh, where the nodes are randomly moved. A small portion of the mesh is shown in Fig. 11.

The same parameters, scheme and number of cells are used. This time, the calculation is performed on the complete domain, without using any symmetry conditions.

The numerical Schlieren at several times are presented in Fig. 12. The results are in good agreement with the previous simulation on a Cartesian grid. One can observe that the shape of the gas cylinders are not perfectly symmetrical with the horizontal axis. This comes from the non-symmetry of the randomly deformed grid. The different waves are, however, well-captured, and the two-phase interface remains sharp.

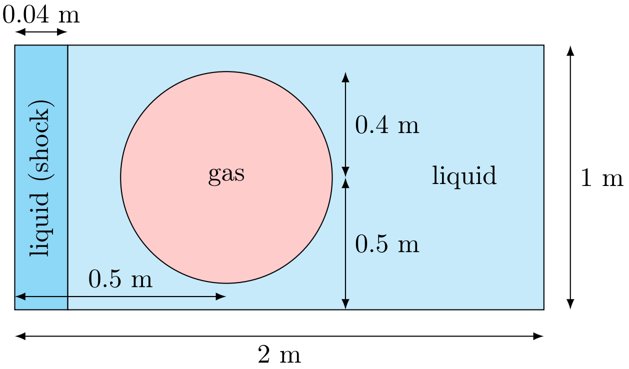

Figure 9: Two-dimensional liquid-gas interaction : geometric description of the test case.

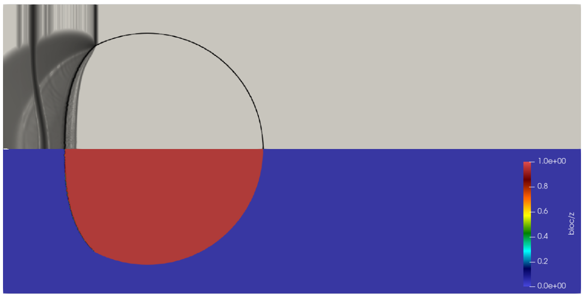

(a) $t = 100\mu s$.

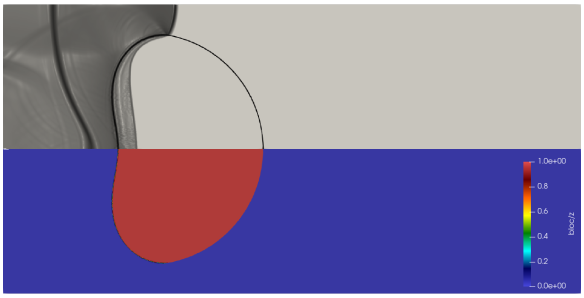

(b) $t = 200\mu s$.

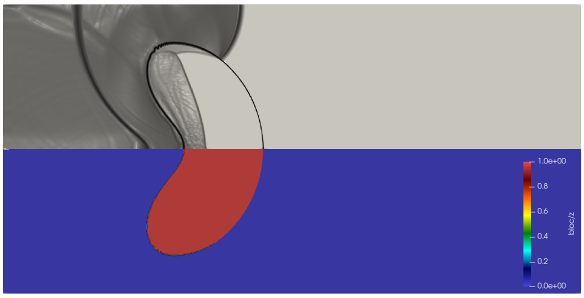

(c) $t = 300\mu s$.

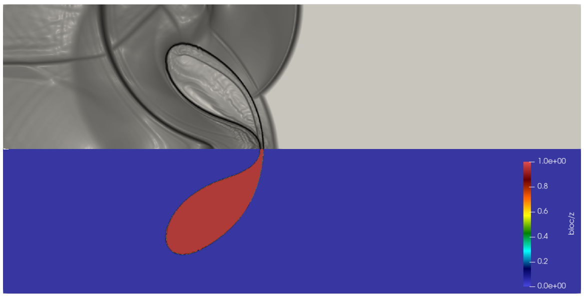

(d) $t = 400\mu s$.

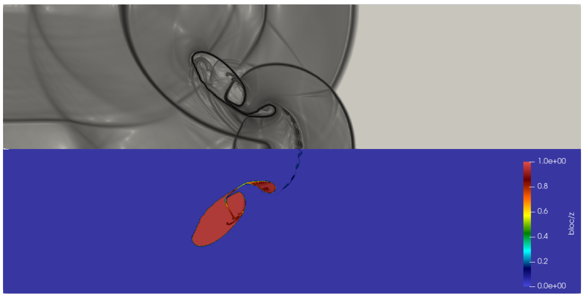

(e) $t = 500\mu s$.

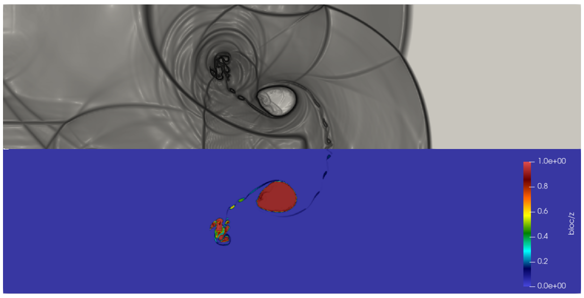

(f) $t = 600\mu s$.

Figure 10: Two-dimensional liquid-gas interaction test case. Numerical Schlieren (upper half) and volume fraction (lower half) at several times.

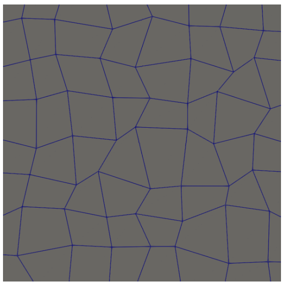

Figure 11: Mesh used for the Two-dimensional liquid-gas interaction on deformed mesh.

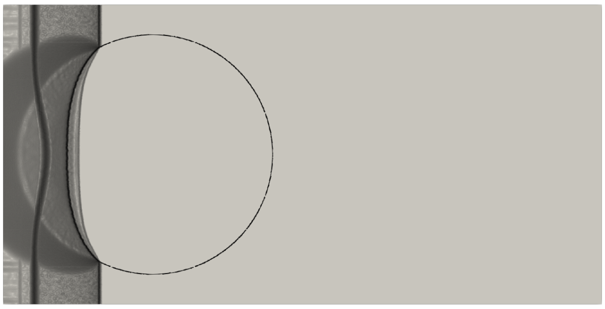

(a) $t = 100\mu s$.

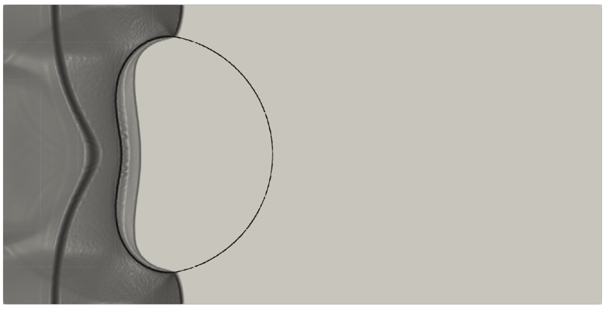

(b) $t = 200\mu s$.

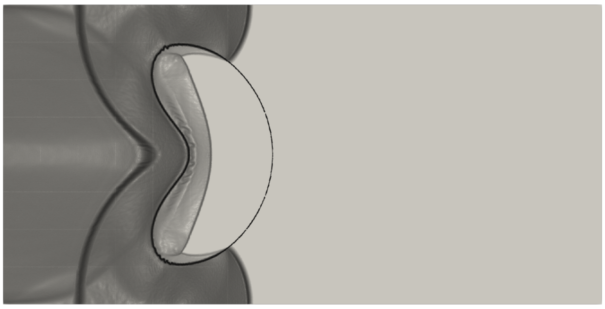

(c) $t = 300\mu s$.

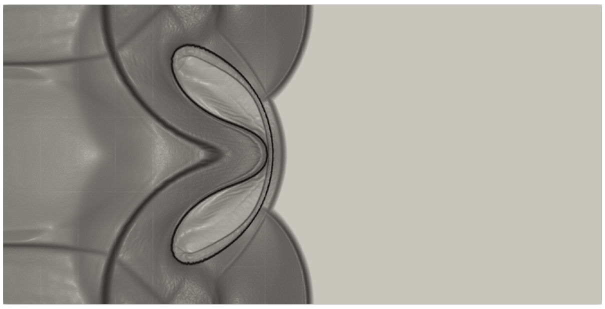

(d) $t = 400\mu s$.

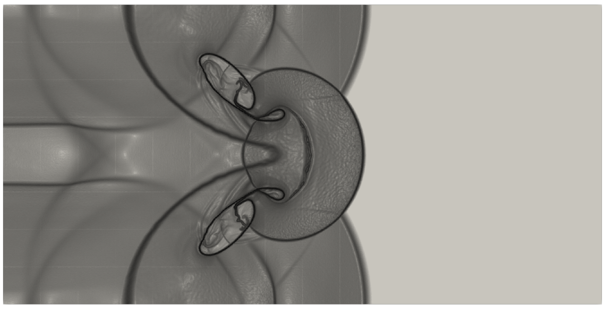

(e) $t = 500\mu s$.

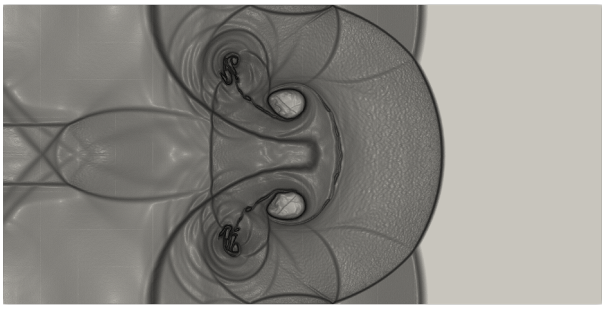

(f) $t = 600\mu s$.

Figure 12: Two-dimensional liquid-gas interaction test case on random mesh. Numerical Schlieren at several times.

5. Conclusion

In this work, several methods for reducing numerical diffusion when studying compressible two-phase flows with immiscible fluids were presented and combined. Since non-miscible fluids are considered, the five-equation system of [2, 35] was used. A robust implicit–explicit acoustic-transport splitting scheme for two-phase flows is used to solve the governing equations. The main contribution of this work is to improve the accuracy of numerical methods used on meshes potentially distorted by ablation. A new and more accurate implicit-explicit time scheme was developed. The second-order extension of the method was performed with a MUSCL-type scheme, that serves to improve the resolution of the numerical scheme. The U-MUSCL scheme [8] with $\kappa = 1/3$ is used, with the correction of [37] for deformed grids. A multidimensional limiter is designed to capture shock and contact discontinuity without oscillations. A β parameter serves to control the compressive property of the limiter, used only on the volume fraction. It sharpens the interface between phases, reduce the numerical diffusion and reproduces finer flow structures. The continuation of this work consists in enriching the model by taking into account capillary effects. These physics will be included in the acoustic step, still with an implicit time-scheme.

Appendix A. Least-squares method

The least-squares method used to compute the local gradient is described in this appendix. We consider the solution α_i in $\mathbf{x}_i$, the center of the cell i. We then define the following linear model

$$\hat{\alpha}_i(\mathbf{x}) = \alpha_i + \boldsymbol{\nabla}\alpha_i.(\mathbf{x} - \mathbf{x}_i). \tag{A.1}$$

The method consists in finding the minimum of the sum

$$S_i = \sum_{j \in v(i)} (\hat{\alpha}_i(\mathbf{x}_j) - \alpha_j)^2, \tag{A.2}$$

where $v(i)$ is a set of neighbors of cell i. The minimization problem (A.2) can be written in the form

$$S_i = ||AX - b||^2 \tag{A.3}$$

with

$$X = \begin{pmatrix} \dfrac{\partial \alpha_i}{\partial x} \\ \dfrac{\partial \alpha_i}{\partial y} \end{pmatrix}, \quad A = \begin{pmatrix} x_{j_1} - x_i & y_{j_1} - y_i \\ x_{j_2} - x_i & y_{j_2} - y_i \\ \vdots & \vdots \\ x_{j_N} - x_i & y_{j_N} - y_i \end{pmatrix} \quad \text{and}$$

$$b = \begin{pmatrix} \alpha_{j_1} - \alpha_i \\ \alpha_{j_2} - \alpha_i \\ \vdots \\ \alpha_{j_N} - \alpha_i \end{pmatrix}.$$

where N is the number of neighboring cells. Thus, finding the minimum of (A.2) consists in finding the minimum of the function $f(\boldsymbol{X}) = ||AX - b||^2$. Its gradient is zero when $AX = b$.

Appendix B. Design of the limiter

In this appendix, the main lines used to obtain the limiter from the inequalities on the local monotonicity preserving principle are detailed.

First, the monotonicity principle is derived. To satisfy the monotonicity principle, the reconstruction of α_i need to hold between $\min_{j \in v(i)}(\alpha_i, \bar{\alpha}_j)$ and $\max_{j \in v(i)}(\alpha_i, \bar{\alpha}_j)$ where $\bar{\alpha}_j$ is the average value between α_i and α_j on their common face. It is such that

$$\frac{\bar{\alpha}_j - \alpha_i}{||\mathbf{x}_{j_k} - \mathbf{x}_i||} = \frac{\alpha_j - \bar{\alpha}_j}{||\mathbf{x}_{j_k} - \mathbf{x}_j||}. \tag{B.1}$$

Thus,

$$\bar{\alpha}_j = \frac{\alpha_i \omega_i + \alpha_j \omega_j}{\omega_i + \omega_j} \tag{B.2}$$

with $\omega_i = ||\mathbf{x}_{j_k} - \mathbf{x}_i||^{-1}$.

Lemma 1
Let $\hat{\alpha}_{ij}$ be the extrapolation of α_i on Γ_{ij} such that

$$\hat{\alpha}_{ij} = \alpha_i + \phi_i \Delta\alpha_{i,j}, \tag{B.3}$$

where ϕ_i is the gradient limiter, and

$$\Delta\alpha_{i,j} = \frac{\kappa}{2}(\alpha_p - \alpha_i) + (1 - \kappa)\boldsymbol{\nabla}\alpha_i.(\mathbf{x}_f - \mathbf{x}_i). \tag{B.4}$$

The reconstruction (B.3) and its symmetrical preserve the monotonicity of the solution i.e.

$$\forall j \in v(i), \ \alpha_i^{\min} \le \alpha_i \pm \phi_i \Delta\alpha_{i,j} \le \alpha_i^{\max}. \tag{B.5}$$

where $\alpha_i^{\min} = \min_{j \in v(i)}(\alpha_i, \bar{\alpha}_j)$, $\alpha_i^{\max} = \max_{j \in v(i)}(\alpha_i, \bar{\alpha}_j)$, the limiter ϕ_i reads

$$\phi_i = \begin{cases} \min\left(\dfrac{\alpha_i - \alpha_i^{min}}{|\Delta\alpha_i|^{\max}}, \dfrac{\alpha_i^{max} - \alpha_i}{|\Delta\alpha_i|^{\max}}\right) & \textit{if } \Delta\alpha_{i,j} \neq 0, \\ 0 & \textit{otherwise}, \end{cases} \tag{B.6}$$

with $|\Delta\alpha_i|^{max} = \max_{j \in v(i)}|\Delta\alpha_{i,j}|$.

Proof. From B.5, we have $\forall j \in v(i)$

$$\begin{cases} \alpha_i^{\min} & \le & \alpha_i + \phi_i \Delta\alpha_{i,j} & \le & \alpha_i^{\max}, \\ \alpha_i^{\min} & \le & \alpha_i - \phi_i \Delta\alpha_{i,j} & \le & \alpha_i^{\max}, \end{cases}$$

which gives

$$\begin{cases} \alpha_i^{\min} - \alpha_i & \le & \phi_i \Delta\alpha_{i,j} & \le & \alpha_i^{\max} - \alpha_i, \\ \alpha_i - \alpha_i^{\max} & \le & \phi_i \Delta\alpha_{i,j} & \le & \alpha_i - \alpha_i^{\min}. \end{cases}$$

Then, two cases should be distinguished

- if $\Delta\alpha_{i,j} > 0$ then

$$\begin{cases} \dfrac{\alpha_i^{\min} - \alpha_i}{\Delta\alpha_{i,j}} & \le & \phi_i & \le & \dfrac{\alpha_i^{\max} - \alpha_i}{\Delta\alpha_{i,j}}, \\ \dfrac{\alpha_i - \alpha_i^{\max}}{\Delta\alpha_{i,j}} & \le & \phi_i & \le & \dfrac{\alpha_i - \alpha_i^{\min}}{\Delta\alpha_{i,j}}, \end{cases}$$

- if $\Delta\alpha_{i,j} < 0$ then

$$\left\{\begin{array}{ccccc} \dfrac{\alpha_i - \alpha_i^{\max}}{|\Delta\alpha_{i,j}|} & \leq & \phi_i & \leq & \dfrac{\alpha_i - \alpha_i^{\min}}{|\Delta\alpha_{i,j}|}, \\ \dfrac{\alpha_i^{\min} - \alpha_i}{|\Delta\alpha_{i,j}|} & \leq & \phi_i & \leq & \dfrac{\alpha_i^{\max} - \alpha_i}{|\Delta\alpha_{i,j}|}. \end{array}\right.$$

Because ϕ_i has to be positive, the left inequalities are always true. The right inequalities have to be true $\forall j \in v(i)$ so the minimum value is chosen. The limiter thus reads

$$\phi_i = \min_{j\in v(i)} \begin{cases} \min\left(\dfrac{\alpha_i^{\max} - \alpha_i}{\Delta\alpha_{i,j}}, \dfrac{\alpha_i - \alpha_i^{\min}}{\Delta\alpha_{i,j}}\right) & \text{if } \Delta\alpha_{i,j} < 0, \\ \min\left(\dfrac{\alpha_i - \alpha_i^{\min}}{|\Delta\alpha_{i,j}|}, \dfrac{\alpha_i^{\max} - \alpha_i}{|\Delta\alpha_{i,j}|}\right) & \text{if } \Delta\alpha_{i,j} > 0, \\ 0 & \text{otherwise,} \end{cases} \tag{B.7}$$

which is equivalent to (B.6). ☐

The constraint $\phi_i \leq 1$ must be added in order to ensure the reconstruction to be exact for linear solution on admissible mesh. The final expression of limiter is thus

$$\phi_i = \begin{cases} \min\left(1, \dfrac{\alpha_i - \alpha_i^{min}}{|\Delta\alpha_i|^{\max}}, \dfrac{\alpha_i^{max} - \alpha_i}{|\Delta\alpha_i|^{\max}}\right) & \text{if } \Delta\alpha_{i,j} \neq 0, \\ 0 & \text{otherwise,} \end{cases} \tag{B.8}$$

Secondly, if the limiter must be compressive, the only condition that need to be satisfy is the maximum principle

$$\forall j, \min_{j\in v(i)}(\alpha_i, \alpha_j) \leq \hat{\alpha}_{ij} \leq \max_{j\in v(i)}(\alpha_i, \alpha_j). \tag{B.9}$$

The limiter is thus

$$\phi_i = \begin{cases} \min\left(\beta, \dfrac{\alpha_i - \alpha_i^{min}}{|\Delta\alpha_i|^{\max}}, \dfrac{\alpha_i^{max} - \alpha_i}{|\Delta\alpha_i|^{\max}}\right) & \text{if } \Delta\alpha_{i,j} \neq 0, \\ 0 & \text{otherwise,} \end{cases} \tag{B.10}$$

with $\alpha_i^{min} = \min_{j\in v(i)}(\alpha_i, \alpha_j)$ and $\alpha_i^{max} = \max_{j\in v(i)}(\alpha_i, \alpha_j)$. The β parameter is added to control the compressive property of the limiter. For the volume fraction which is theoretically piecewise constant, preservation of the maximum principle is the only desired property. It is not necessary to preserve the linearity of the solution so $\beta > 1$ can be employed.

Appendix C. Truncation error of implicit acoustic time-schemes

In this appendix, the calculation of the truncation error of both implicit time-scheme used for the acoustic step (2.10) is detailed.

Lemma 2
The truncation error of the implicit time-scheme (2.13) *that reads*

$$\frac{\boldsymbol{V}^{n+1} - \boldsymbol{V}^n}{\Delta t} = -\vartheta^n \nabla \cdot \boldsymbol{G}(\boldsymbol{V}^{n+1}), \tag{C.1}$$

is given by

$$\tau^n = \Delta t \left[\frac{\partial_t^2 \boldsymbol{V}(t)}{2} + \vartheta(t)\nabla \cdot \partial_t \boldsymbol{G}(\boldsymbol{V}(t))\right] + O(\Delta t^2), \tag{C.2}$$

while the truncation error of the modified Crank-Nicolson time-scheme (3.15) *that reads*

$$\frac{\boldsymbol{V}^{n+1} - \boldsymbol{V}^n}{\Delta t} = -\frac{1}{2}\vartheta^n \left(\nabla \cdot \boldsymbol{G}(\boldsymbol{V}^n) + \nabla \cdot \boldsymbol{G}(\boldsymbol{V}^{n+1})\right), \tag{C.3}$$

is given by

$$\tau^n = \Delta t \left[\frac{\partial_t^2 \boldsymbol{V}(t)}{2} + \frac{\vartheta(t)\nabla \cdot \partial_t \boldsymbol{G}(\boldsymbol{V}(t))}{2}\right] + O(\Delta t^2). \tag{C.4}$$

Proof. The truncation error of the first implicit time-scheme scheme is

$$\begin{aligned} \tau^n &= \frac{\boldsymbol{V}(t+\Delta t) - \boldsymbol{V}(t)}{\Delta t} + \vartheta(t)\nabla \cdot \boldsymbol{G}(\boldsymbol{V}(t+\Delta t)), \\ &= \partial_t \boldsymbol{V}(t) + \frac{\Delta t}{2}\partial_t^2 \boldsymbol{V}(t) + \vartheta(t)\nabla \cdot \boldsymbol{G}(\boldsymbol{V}(t) \\ &\quad + \Delta t \nabla \cdot (\partial_t \boldsymbol{G}(\boldsymbol{V}(t))) + O(\Delta t^2), \\ &= \Delta t \left[\frac{\partial_t^2 \boldsymbol{V}(t)}{2} + \vartheta(t)\nabla \cdot \partial_t \boldsymbol{G}(\boldsymbol{V}(t))\right] + O(\Delta t^2). \end{aligned} \tag{C.5}$$

The truncation error of the modified Crank-Nicolson scheme is

$$\begin{aligned} \tau^n &= \frac{\boldsymbol{V}(t+\Delta t) - \boldsymbol{V}(t)}{\Delta t} \\ &\quad + \frac{1}{2}\vartheta(t)\left(\nabla \cdot \boldsymbol{G}(\boldsymbol{V}(t+\Delta t)) + \nabla \cdot \boldsymbol{G}(\boldsymbol{V}(t))\right), \\ &= \partial_t \boldsymbol{V}(t) + \frac{\Delta t}{2}\partial_t^2 \boldsymbol{V}(t) + \vartheta(t)\nabla \cdot \boldsymbol{G}(\boldsymbol{V}(t) \\ &\quad + \frac{\Delta t}{2}\nabla \cdot (\partial_t \boldsymbol{G}(\boldsymbol{V}(t))) + O(\Delta t^2), \\ &= \frac{\Delta t}{2}\left[\partial_t^2 \boldsymbol{V}(t) + \vartheta(t)\nabla \cdot \partial_t \boldsymbol{G}(\boldsymbol{V}(t))\right] + O(\Delta t^2). \end{aligned} \tag{C.6}$$

☐

From the truncation errors calculated earlier, one can see that the new implicit scheme, called the modified Crank-Nicolson scheme, produces a smaller error than the first implicit scheme. We then expect to achieve more accurate numerical results with the second scheme.

References

[1] Ahn, H., Shashkov, M., 2007. Multi-material interface reconstruction on generalized polyhedral meshes. J. Comput. Phys. 226, 2096–2132.

[2] Allaire, G., Clerc, S., Kokh, S., 2002. A five-equation model for the simulation of interfaces between compressible fluids. J. Comput. Phys. 181, 577–616.

[3] Anderson, D.M., McFadden, G.B., Wheeler, A.A., 1998. Diffuse-Interface Methods in Fluid Mechanics. Annual Review of Fluid Mechanics 30, 139–165. doi:`10.1146/annurev.fluid.30.1.139`.

[4] Baer, M., Nunziato, J., 1986. A two-phase mixture theory for the deflagration-to-detonation transition (DDT) in reactive granular materials. Int. J. Multiphase Flow 12, 861–889.

[5] Barth, T., Jespersen, D.C., 1989. The design and application of upwind schemes on unstructured meshes. AIAA Paper 89-0366 .

[6] Berthon, C., 2005. Stability of the MUSCL Schemes for the Euler Equations. Commun. Math. Sci. 3.

[7] Blanchard, G., 2015. Modélisation et simulation multi-échelles de l'atomisation d'une nappe liquide cisaillée. Ph.D. thesis. Université de Toulouse.

[8] Burg, C., 2005. Higher Order Variable Extrapolation for Unstructured Finite Volume RANS Flow Solvers. AIAA Paper 2005-4999 .

[9] Caramana, E., Shashkov, M., 1998. Elimination of Artificial Grid Distortion and Hourglass-Type Motions by Means of Lagrangian Subzonal Masses and Pressures. J. Comput. Phys. 142, 521–561. URL: https://www.sciencedirect.com/science/article/pii/S0021999198959526, doi:https://doi.org/10.1006/jcph.1998.5952.

[10] Chalons, C., Girardin, M., Kokh, S., 2016. An all-regime Lagrange-Projection like scheme for the gas dynamics equations on unstructured meshes. Comm. Comput. Phys. 20, 188–233.

[11] Chalons, C., Girardin, M., Kokh, S., 2017. An all-regime Lagrange-Projection like scheme for 2D homogeneous models for two-phase flows on unstructured meshes. J. Comput. Phys. 335, 885–904. URL: https://www.sciencedirect.com/science/article/pii/S002199911730027X, doi:https://doi.org/10.1016/j.jcp.2017.01.017.

[12] Chan, A., Gallice, G., Loubère, R., Maire, P.H., 2021. Positivity preserving and entropy consistent approximate Riemann solvers dedicated to the high-order MOOD-based Finite Volume discretization of Lagrangian and Eulerian gas dynamics. Comput. Fluids 229, 105056. URL: https://www.sciencedirect.com/science/article/pii/S0045793021002206, doi:https://doi.org/10.1016/j.compfluid.2021.105056.

[13] Chanteperdrix, G., Villedieu, P., Vila, J., 2002. A Compressible Model for Separated Two-Phase Flows Computations Volume 1: Fora, Parts A and B, 809–816.

[14] Cheng, L., Deng, X., Xie, B., Jiang, Y., Xiao, F., 2021. Low-dissipation BVD schemes for single and multi-phase compressible flows on unstructured grids. J. Comput. Phys. 428, 110088.

[15] Chiapolino, A., Saurel, A., Nkonga, B., 2017. Sharpening diffuse interfaces with compressible fluids on unstructured meshes. J. Comput. Phys. 340, 389–417. URL: https://www.sciencedirect.com/science/article/pii/S0021999117302371, doi:https://doi.org/10.1016/j.jcp.2017.03.042.

[16] De Vuyst, F., Fochesato, C., Mahy, V., Motte, R., Peybernes, M., 2021. A geometrically accurate low-diffusive conservative interface capturing method suitable for multimaterial flows. Comput. Fluids , 104897URL: https://www.sciencedirect.com/science/article/pii/S0045793021000633, doi:https://doi.org/10.1016/j.compfluid.2021.104897.

[17] Deng, X., Inaba, S., Xie, B., Shyue, K., Xiao, F., 2018. High fidelity discontinuity-resolving reconstruction for compressible multiphase flows with moving interfaces. J. Comput. Phys. 371, 945–966. doi:https://doi.org/10.1016/j.jcp.2018.03.036.

[18] Després, B., Lagoutière, F., 2002. Contact discontinuity capturing schemes for linear advection and compressible gas dynamics. J. Sci. Comput 16, 16–479.

[19] Flåtten, T., Lund, H., 2011. Relaxation two-phase flow models and the subcharacteristic condition. Mathematical Models and Methods in Applied Sciences 21, 2379–2407. doi:10.1142/S0218202511005775.

[20] Friess, M.B., Boutin, B., Caetano, F., Faccanoni, G., Kokh, S., Lagoutière, F., Navoret, L., 2011. A second order anti-diffusive Lagrange-remap scheme for two-component flows. ESAIM: Proc. 32, 149–162.

[21] Gallice, G., 2003. Positive and entropy stable Godunov-type schemes for gas dynamics and MHD equations in Lagrangian or Eulerian coordinates. Numerische Mathematik 94, 673–713.

[22] Gander, W., 2003. Algorithms for the QR-Decomposition .

[23] Grenier, N., Vila, J.P., Villedieu, P., 2013. An accurate low-mach scheme for a compressible two-fluid model applied to free-surface flows. J. Comput. Phys. 252, 1–19. URL: https://www.sciencedirect.com/science/article/pii/S0021999113004312, doi:https://doi.org/10.1016/j.jcp.2013.06.008.

[24] Haas, J.F., Sturtevant, B., 1987. Interaction of weak shock waves with cylindrical and spherical gas inhomogeneities. J. Fluid Mech. 181, 41–76.

[25] Heider, Y., 2021. A review on phase-field modeling of hydraulic fracturing. Engineering Fracture Mechanics 253, 107881. doi:10.1016/j.engfracmech.2021.107881.

[26] Helluy, P., Jung, J., 2013. OpenCL numerical simulations of two-fluid compressible flows with a 2D random choice method. IJFV 10, 1–38.

[27] Hirt, C., Nichols, B., 1981. Volume of fluid (VOF) method for the dynamics of free boundaries. J. Comput. Phys. 39, 201–225. URL: https://www.sciencedirect.com/science/article/pii/0021999181901455, doi:https://doi.org/10.1016/0021-9991(81)90145-5.

[28] Jung, J., 2013. Schémas numériques adaptés aux accélérateurs multicœurs pour les écoulements bifluide. Ph.D. thesis. Université de Strasbourg.

[29] Kapila, A., Menikoff, R., Bdzil, J., Son, S., Stewart, D.S., 2001. Two-phase modeling of deflagration-to-detonation transition in granular materials: Reduced equations. Phys. Fluids 13, 3002–3024.

[30] Kokh, S., Lagoutière, F., 2010. An anti-diffusive numerical scheme for the simulation of interfaces between compressible fluids by means of five-equation model. J. Comput. Phys. 229, 2773–2809.

[31] Kreeft, J., Koren, B., 2010. A new formulation of Kapila's five-equation model for compressible two-fluid flow, and its numerical treatment. J. Comput. Phys. 229, 6220–6242.

[32] van Leer, B., 1979. Towards the ultimate conservative difference scheme. V. A second-order sequel to Godunov's method. J. Comput. Phys. 32, 101–136.

[33] Lund, H., 2012. A hierarchy of relaxation models for two-phase flow. SIAM J. App. Math. 72, 1713–1741. doi:10.1137/12086368X.

[34] Maire, P.H., Abgrall, R., Breil, J., Ovadia, J., 2007. A cell-centered lagrangian scheme for two-dimensional compressible flow problems. SIAM J. Sci. Comput. 29, 1781–1824.

[35] Massoni, J., Saurel, R., Nkonga, B., Abgrall, R., 2002. Some models and Eulerian methods for interface problems between compressible fluids with heat transfer. Int. J. Heat Mass Transfer 45, 1287–1307.

[36] Murrone, A., Guillard, H., 2005. A five equation reduced model for compressible two phase flow problems. J. Comput. Phys. 202, 664 – 698. URL: http://www.sciencedirect.com/science/article/pii/S0021999104003018.

[37] Nishikawa, H., 2020. On the loss and recovery of second-order accuracy with U-MUSCL. J. Comput. Phys. 417, 109600.

[38] Osher, S., Sethian, J., 1988. Fronts propagating with curvature-dependent speed: Algorithms based on Hamilton-Jacobi formulations. J. Comput. Phys. 79, 12–49. URL: https://www.sciencedirect.com/science/article/pii/0021999188900022, doi:https://doi.org/10.1016/0021-9991(88)90002-2.

[39] Padway, E., Nishikawa, H., . Resolving Confusion Over Third-Order Accuracy of U-MUSCL.

[40] Peluchon, S., Gallice, G., Mieussens, L., 2017. A robust implicit–explicit acoustic-transport splitting scheme for two-phase flows. J. Comput. Phys. 339, 328–355.

[41] Peluchon, S., Gallice, G., Mieussens, L., 2021. Development of numerical methods to simulate the melting of a thermal protection system. J. Comput. Phys. , 110753URL: https://www.sciencedirect.com/science/article/pii/S0021999121006483, doi:https://doi.org/10.1016/j.jcp.2021.110753.

[42] Qian, L., Causon, D., Mingham, C., Ingram, D., 2006. A free-surface capturing method for two fluid flows with moving bodies. Proc. R. Soc. A. 462, 21–42. doi:10.1098/rspa.2005.1528.

[43] Rider, W., Kothe, D., 1998. Reconstructing Volume Tracking. J. Comput. Phys. 141, 112–152. doi:10.1006/jcph.1998.5906.

[44] Saurel, R., Abgrall, R., 1999. A simple method for compressible multifluid flows. SIAM J. Sci. Comput. 21 (3), 1115–1145.

[45] Saurel, R., Petitpas, F., Berry, R., 2009. Simple and efficient relaxation methods for interfaces separating compressible fluids, cavitating flows and shocks in multiphase mixtures. J. Comput. Phys. 228, 1678–1712. URL: https://www.sciencedirect.com/science/article/pii/S0021999108005895, doi:https://doi.org/10.1016/j.jcp.2008.11.002.

[46] Shyue, K., 2006. A wave-propagation based volume tracking method for compressible multicomponent flow in two space dimensions. J. Comput. Phys. 215, 219–244.

[47] Shyue, K., Xiao, F., 2014. An Eulerian interface sharpening algorithm for compressible two-phase flow: The algebraic THINC approach. J. Comput. Phys. 268, 326–354.

[48] Sun, Z., Inaba, S., Xiao, F., 2016. Boundary variation diminishing (BVD) reconstruction: A new approach to improve Godunov schemes. J. Comput. Phys. 322, 309–325. URL: https://www.sciencedirect.com/science/article/pii/S0021999116302765, doi:https://doi.org/10.1016/j.jcp.2016.06.051.

[49] Syrakos, A., Varchanis, S., Dimakopoulos, Y., Goulas, A., Tsamopoulos, J., 2017. A critical analysis of some popular methods for the discretisation of the gradient operator in finite volume methods. Phys. Fluids 29, 127103. doi:10.1063/1.4997682.

[50] Toro, E., 1997. Riemann solvers and Numerical Methods for Fluid Dynamics. Springer.

[51] Vilar, F., Shu, C., Maire, P.H., 2016. Positivity-preserving cell-centered lagrangian schemes for multi-material compressible flows: From first-order to high-order. Part I: The one-dimensional case. J. Comput. Phys. .

[52] VonNeumann, J., Richtmyer, R.D., 1950. A method for the numerical calculation of hydrodynamic shocks. J. App. Phys. 21, 232–237. URL: https://doi.org/10.1063/1.1699639, doi:10.1063/1.1699639, arXiv:https://doi.org/10.1063/1.1699639.

[53] Xiao, F., Honma, Y., Kono, T., 2005. A simple algebraic interface capturing scheme using hyperbolic tangent function. Int. J. Numer. Methods Fluids 48, 1023 – 1040. doi:10.1002/fld.975.

[54] Zalesak, S., 1979. Fully multidimensional flux-corrected transport algorithms for fluids. J. Comput. Phys. 31, 335–362. URL: https://www.sciencedirect.com/science/article/pii/0021999179900512, doi:https://doi.org/10.1016/0021-9991(79)90051-2.